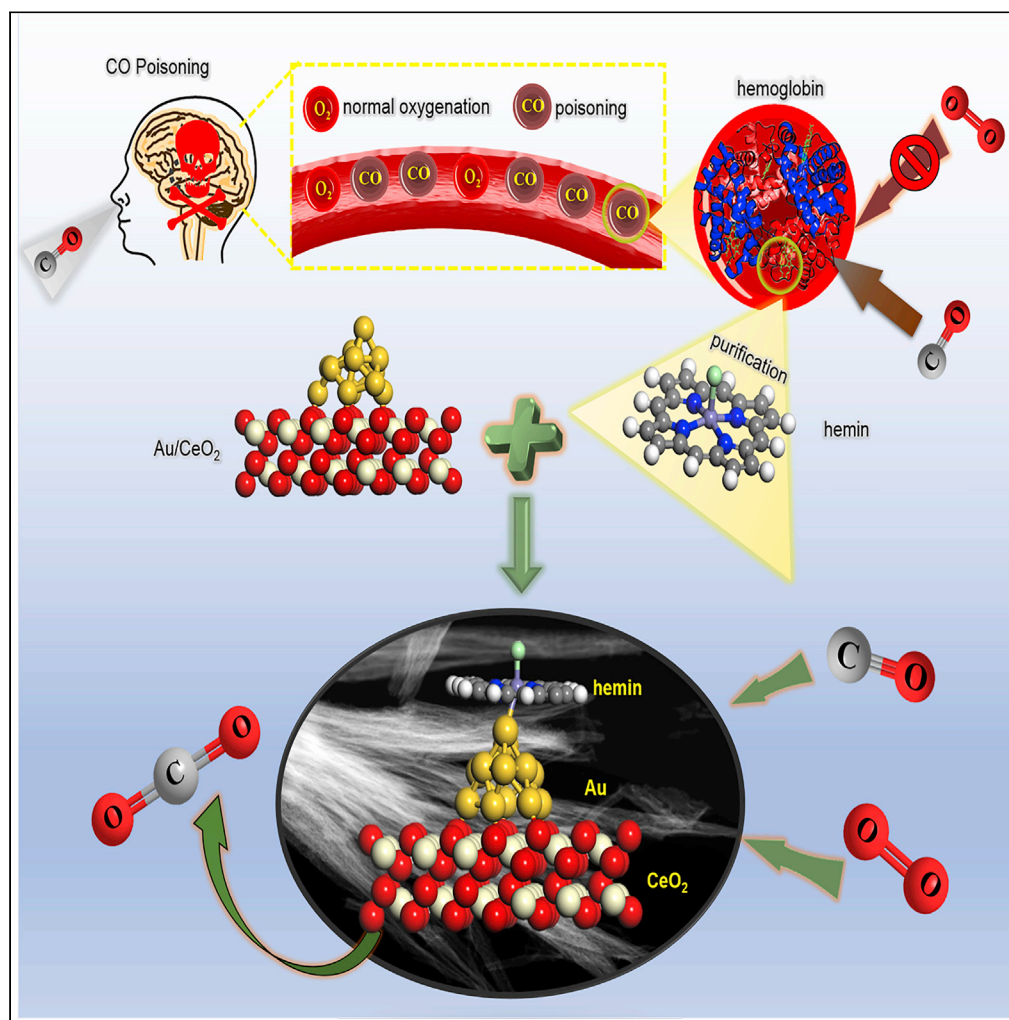


Article

Biomimetic Au/CeO₂ Catalysts Decorated with Hemin or Ferrous Phthalocyanine for Improved CO Oxidation via Local Synergistic Effects

Longlong Fan,
Jiajun Dai,
Zhongliang
Huang, ..., Jiale
Huang, Shu-Feng
Zhou, Guowu Zhan

cola@xmu.edu.cn (J.H.)
szhou@hqu.edu.cn (S.-F.Z.)
gwzhan@hqu.edu.cn (G.Z.)

HIGHLIGHTS

Biomimetic catalysts were prepared by the integration of biomolecules with Au/CeO₂

The experimental TOF of hemin-Au/CeO₂ was ca. 30 times higher than that of Au/CeO₂

Strong electronic interactions facilitate the adsorption and activation of CO molecule

DFT calculations reveal the mechanisms of enhanced activity of biomimetic catalysts

Fan et al., iScience 23, 101852
December 18, 2020 © 2020
The Author(s).
<https://doi.org/10.1016/j.isci.2020.101852>

Article

Biomimetic Au/CeO₂ Catalysts Decorated with Hemin or Ferrous Phthalocyanine for Improved CO Oxidation via Local Synergistic Effects

Longlong Fan,^{1,4} Jiajun Dai,^{2,4} Zhongliang Huang,¹ Jingran Xiao,¹ Qingbiao Li,^{2,3} Jiale Huang,^{2,*} Shu-Feng Zhou,^{1,*} and Guowu Zhan^{1,5,*}

SUMMARY

Biomimetic catalysts have drawn broad research interest owing to both high specificity and excellent catalytic activity. Herein, we report a series of biomimetic catalysts by the integration of biomolecules (hemin or ferrous phthalocyanine) onto well-defined Au/CeO₂, which leads to the high-performance CO oxidation catalysts. Strong electronic interactions among the biomolecule, Au, and CeO₂ were confirmed, and the CO uptake over hemin-Au/CeO₂ was roughly about 8 times greater than Au/CeO₂. Based on the Au/CeO₂(111) and hemin-Au/CeO₂(111) models, the density functional theory calculations reveal the mechanisms of the biomolecules-assisted catalysis process. The theoretical prediction suggests that CO and O₂ molecules preferentially bind to the surface of noncontacting Au atoms (low-coordinated sites) rather than the biomolecule sites, and the accelerating oxidation of Au-bound CO occurs via either the Langmuir-Hinshelwood mechanism or the Mars-van Krevelen mechanism. Accordingly, the findings provide useful insights into developing biomimetic catalysts with low cost and high activity.

INTRODUCTION

To date, biomimicry not only provides a novel perspective on how nature works but also brings inspiration into the design and synthesis of materials with a variety of biomimetic functions (Decréau et al., 2010). As an exciting branch of biomimicry, biomimetic catalysts inspired by nature enzymes have been extensively studied in a wide variety of reaction processes, including CO₂ photoreduction (Chen et al., 2019), oxygen reduction (Wei et al., 2014), pyrogallol oxidation (Xue et al., 2012), aerobic glucose oxidation (Tegeeder et al., 2018), water splitting (Yu et al., 2013), organic syntheses (Marchetti and Levine, 2011), and so forth. Due to the fragile nature and high cost of enzymes, the catalytically active components in enzymes such as metalloporphyrins and metallosalens molecules have been utilized to fabricate highly efficient biomimetic catalysts for imitating diverse biological systems, e.g., peroxidase, hemoglobin, and cytochrome P450 (Gu et al., 2014). Compared with parent enzymes, biomimetic catalysts decorated with pretty cheap biomolecules not only own significantly enhanced stability but also retain ecofriendly, high-efficiency, and unique specificity properties (Li et al., 2017; Lian et al., 2019).

Among the various biomolecules, hemin is a reactive ferric protoporphyrin-IX produced from hemoglobin molecule being responsive for selective binding and transfer of O₂ in the blood of animals (Li et al., 2017). It is worth mentioning that CO is responsible for fatal poisoning due to 220% greater affinity for CO to hemoglobin (forming carboxyhemoglobin) than O₂ (forming oxyhemoglobin), causing cellular hypoxia. Although hemin (Fe^{III}) has a relatively weaker interaction with CO than the reduced hemin (Fe^{II}) (Savagatrup et al., 2017), it is stable in the ambient atmosphere and commercially available at a relatively low price, which could be functionalized on various substrates, e.g., Au electrodes (Ma et al., 2007), graphenes (Guo et al., 2011), carbon powders (Liang et al., 2011), carbon nanotubes (Zhang et al., 2015), and so forth. The binding of biomolecules on biomimetic catalysts can be realized by metal coordination, hydrogen bonding, Lewis acid-base coordination, van der Waals and dipole-dipole interactions, etc. (Breslow, 1995; Wu et al., 2019). Nevertheless, to our knowledge, the construction of biomimetic systems based on hemin molecules being eligible for CO catalytic oxidation has scarcely been reported.

¹College of Chemical Engineering, Integrated Nanocatalysts Institute (INCI), Huaqiao University, 668 Jimei Avenue, Xiamen, Fujian, 361021, P. R. China

²Department of Chemical and Biochemical Engineering, College of Chemistry and Chemical Engineering, Xiamen University, 422 South Siming Road, Xiamen, Fujian, 361005, P. R. China

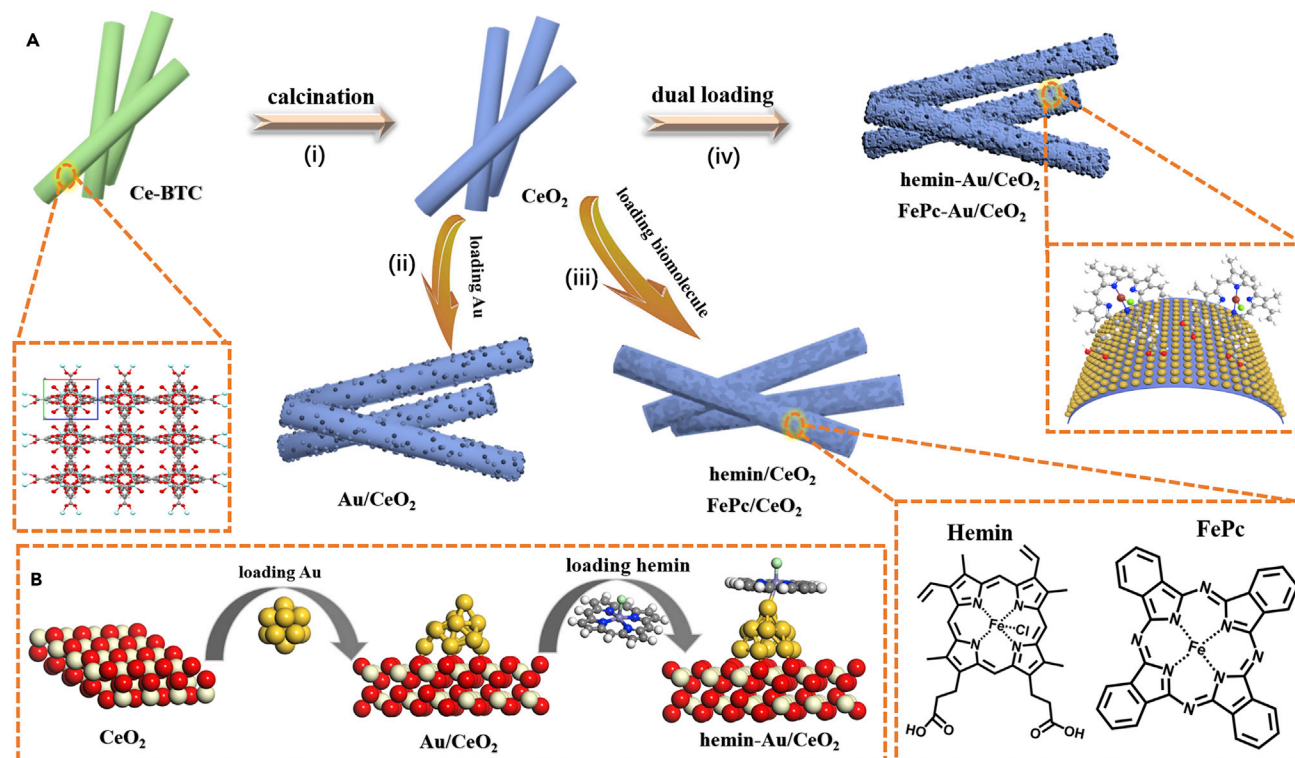
³College of Food and Biology Engineering, Jimei University, Xiamen, Fujian 361021, P. R. China

⁴These authors contributed equally

⁵Lead Contact

*Correspondence: cola@xmu.edu.cn (J.H.), szhou@hqu.edu.cn (S.-F.Z.), gwzhan@hqu.edu.cn (G.Z.)
<https://doi.org/10.1016/j.isci.2020.101852>





Scheme 1. Synthetic Routes of the Catalysts and Their Structural Models

(A) Schematic diagram of the diverse synthetic routes and (B) geometric structures of CeO_2 , Au/CeO_2 , and hemin-Au/CeO_2 used in DFT calculations

The catalytic oxidation of CO to CO_2 is not only an archetypal heterogeneous reaction for fundamental studies but also an important reaction for several practical processes, such as fuel cell applications (CO removal from H_2 steam) (Alayoglu et al., 2008) and automotive emission control (Allian et al., 2011). Although many metal catalysts (Au, Pt, Pd, Rh, etc.) have exhibited 100% CO conversion at a temperature of 200°C and above, they suffer from CO poisoning at lower temperatures with a limited reactivity. Therefore, most vehicle exhaust pollutants are usually emitted during the warming up of the three-way catalytic converter as starting the car (<30 s) (Peterson et al., 2014). It remains a daunting challenge to develop catalysts that are not poisoned by CO and readily active at low temperatures. Based on the Sabatier principle, CO bonding on the catalyst too weakly or too strongly is not feasible for the reaction, thereby a modest binding strength for CO is highly desirable. Therefore, the direct usage of hemin is not suitable for low-temperature CO oxidation due to preferential adsorption of CO over O_2 . Besides, one major challenge of the direct application of hemin is the aggregation in aqueous solution to form catalytic inactive dimers and oxidative self-destruction in the oxidizing media, which fails to achieve the biological self-assembly (Xue et al., 2012). Accordingly, it has been speculated that hemin-supported biomimetic catalysts for facile CO oxidation should rely on at least three major conditions: (1) the binding of monomeric hemin on a substrate (preferably with a large surface area), (2) an additional component guaranteeing high oxygen storage and release capacity (e.g., CeO_2 support) as the hemin cannot adsorb oxygen in the presence of CO, and (3) a synergistic effect between multiple sites for CO activation and conversion.

With these considerations in mind, herein, a series of biomimetic catalysts were developed by loading of hemin (or its analog ferrous phthalocyanine, FePc) on well-defined Au/CeO_2 . The CeO_2 support was fabricated by a thermal transformation strategy with Ce-BTC as a precursor (cerium-based metal-organic frameworks) based on our previous work (Fan et al., 2019), which displayed the nanorod morphology and a large surface area, being beneficial for loading guest active components. To do this, the synthetic strategy can be divided into two steps as shown in Scheme 1A: (i) synthesis of CeO_2 from the pyrolysis of Ce-BTC nanorods and (ii–iv) individually or simultaneously loading Au

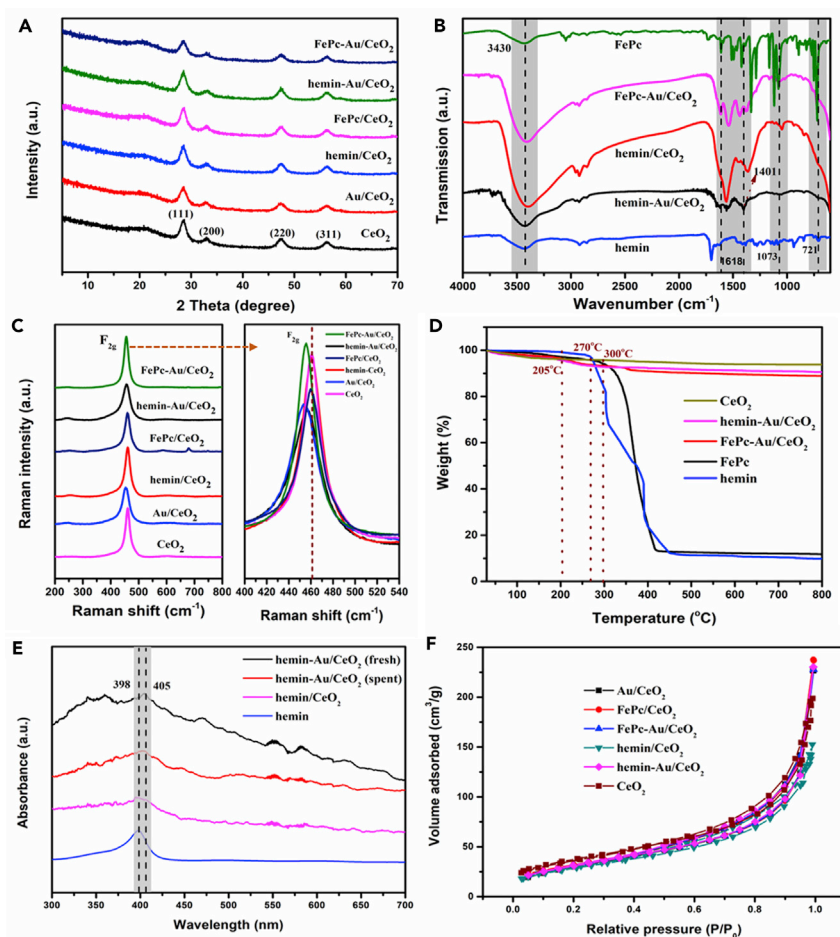


Figure 1. Characterization Results of the Catalyst Samples

(A) X-ray diffraction patterns, (B) Fourier transform infrared spectra, (C) Raman spectra, (D) thermogravimetric analysis profiles, (E) UV-visible spectra, and (F) N_2 physisorption isotherms.

nanoparticles and biological macromolecules (hemin and FePc) on the porous CeO_2 nanorods through the wet-chemical assembly. Systematic physicochemical characterizations were applied to check the successful combination of multiple components on the integrated catalyst system. We then evaluated the catalytic performance of the hemin (or FePc)-loaded Au/CeO_2 catalysts for CO oxidation. Operando DRIFTS was used to elucidate the nature of the active sites of catalysts under reaction conditions. Furthermore, the theoretical density functional theory (DFT) calculations provide key insights into the structure-function relationship for a comprehensive understanding of catalytic mechanisms.

RESULTS AND DISCUSSION

Characterization of the Biomimetic Catalysts

As shown in Figure 1A, all the catalysts exhibited strong diffractions at 28.3° , 33.1° , 47.4° , and 56.3° , corresponding to (111), (200), (220), and (311) of CeO_2 with cubic fluorite structure (JCDPS 81-0792) (Fan et al., 2019). No obvious diffraction peaks belonging to Au or biomolecules were found probably due to the low loading amount and the high dispersion. Fourier transform infrared spectroscopic characterization further confirmed the presence of organic biomolecules (hemin or FePc) bound to the catalyst surface (Figure 1B). As can be seen, the samples were featured with the characteristic of C=C/C=N stretching vibration (at $1,618\text{ cm}^{-1}$) on the protoporphyrin ring and a pair of signals appeared at $1,073$ and 721 cm^{-1} were corresponding to C–N and C–H vibrations, respectively (Luo et al., 2019; Wang et al., 2016). As displayed in

Figure 1C, all the samples presented a strong peak at around 460 cm^{-1} belonging to Raman active F_{2g} of CeO_2 . There was a small downshift of the F_{2g} peak of the biomimetic catalyst compared with the pristine CeO_2 support, which reflected the enriched oxygen vacancies, probably due to the strong interaction between the guest (Au or biomolecules) and CeO_2 (vide infra) (Lee et al., 2011). As shown from the thermogravimetric analysis profiles in Figure 1D, the weight loss before 150°C can be assigned to the presence of moisture. Moreover, a dramatic weight loss of $\sim 85\%$ starting at 270°C (or 300°C) was caused by the decomposition of hemin (or FePc), which was completed as the temperature exceeds 450°C . Interestingly, the decomposition of biomolecules was promoted to 200°C in the presence of Au, which is due to the catalytic effect of Au on organic matter decomposition (Zhan and Zeng, 2018). Accordingly, in our work, a maximum temperature of 170°C was chosen for the pretreatment and the reaction. Moreover, inductively coupled plasma-optical emission spectroscopy (ICP-OES) measurement indicated that the Fe loading amounts on hemin-Au/ CeO_2 , FePc-Au/ CeO_2 , and hemin/ CeO_2 were 0.17, 0.21, and 0.18 wt %, respectively. Therefore, the loading amounts of biomolecules on the three biomimetic catalysts were 1.98, 2.13, and 2.09 wt %, respectively. The biomimetic catalysts appeared to be light gray and light green color after loading hemin and FePc, respectively, which were distinctly different from the light yellow color of CeO_2 and pale pink color of Au/ CeO_2 (see Figure S1 and Supplemental Information).

UV-visible absorption spectra further verify the existence of hemin in the catalyst samples. As shown in Figure 1E, the methanolic suspension of the samples exhibited nearly the same absorption peaks at around 398 nm due to the Soret band of monomeric hemin, in accordance with the reported work (Guo et al., 2011). Moreover, it can be clearly observed that the Soret band in the supported samples (hemin-Au/ CeO_2 and hemin/ CeO_2) slightly red-shifted from 398 to 405 nm, compared with the free hemin, likely due to the formation of conjugate via interactions between iron centers in hemin and the support. In addition, all the catalyst samples showed type IV N_2 physisorption isotherms with a small hysteresis loop due to the capillary condensation of mesopores (Figure 1F), suggesting that both Au and biomolecules did not block the porosity of CeO_2 (Tan et al., 2019). The specific Brunauer-Emmett-Teller surface areas (S_{BET}) were calculated to be 113, 114, 104, 116, and $113\text{ m}^2/\text{g}$ for hemin-Au/ CeO_2 , FePc-Au/ CeO_2 , hemin/ CeO_2 , FePc/ CeO_2 , and Au/ CeO_2 , respectively, which were only slightly lower than that of pure CeO_2 ($133\text{ m}^2/\text{g}$). The average pore sizes of these catalysts all ranged between 3.5 and 4 nm (Figure S2 and Supplemental Information), following in a mesoporous range.

As shown from transmission electron microscopic (TEM) (Figure 2) and scanning electron microscopic (SEM) (Figure S3 and Supplemental Information) images, all the CeO_2 -supported samples showed a rod-like morphology (with length $>4\text{ }\mu\text{m}$) with a rough surface, which was spontaneously assembled in stacking bundles. The morphology is quite similar to the original Ce-BTC (Figure S4 and Supplemental Information). With careful observation, the high-angle annular dark-field scanning transmission electron microscopy (HAADF-STEM) images (Figures 2B, 2F, 2J and S5 and Supplemental Information) clearly display the porous feature of the nanorods formed from a large number of nanocrystals (size of 5 nm) joined together, similar to the X-ray diffraction results (grain sizes of 5.5 nm from Scherrer's equation). The distinguished shining spots in the HAADF-STEM image resulted from Au (due to the higher atomic number $Z_{\text{Au}} = 79$) confirming that Au nanoparticles were uniformly dispersed on the support. The average size of Au nanoparticles in Au/ CeO_2 , hemin-Au/ CeO_2 , and FePc-Au/ CeO_2 were measured to be 5.6, 2.5, and 3.0 nm, respectively. Some larger Au crystallites were found in Au/ CeO_2 sample, as denoted by the dashed red circles in Figure 2B. It suggests that the addition of biomolecules can reduce the size of Au nanoparticles, probably due to the high interactions between biomolecule and Au (vide infra). Besides, the Au loading amounts on Au/ CeO_2 , hemin-Au/ CeO_2 , and FePc-Au/ CeO_2 were determined by ICP-OES as 0.9, 0.9, 1.0 wt %, respectively. As expected, the interplanar spacing distances of 0.24 and 0.32 nm belonging to the (111) plane of fcc Au and (110) plane of CeO_2 , respectively, were observed in the high-resolution TEM images (Figures 2D, 2H, and 2I). The polycrystalline nature was convinced by the selected area electron diffraction pattern (inset in Figures 2G and S6 and Supplemental Information). Furthermore, energy-dispersive X-ray spectroscopic elemental maps clearly show the high level of dispersion of Au and Fe (from the decorated biomolecules) on the CeO_2 support (Figure 2M).

As shown in Figure 3A, the X-ray photoelectron spectroscopic (XPS) images in the C 1s region could be fitted by four distinct peaks. Apart from the sp^3 hydrocarbon with binding energy (B.E.) of 284.8 eV, the other three characteristic peaks at B.E. of 283.8, 286.1, 288.6 eV were corresponding to the C=C, N-C=N, and carboxylic groups in hemin, respectively (Liang et al., 2019; Wang et al., 2013), further

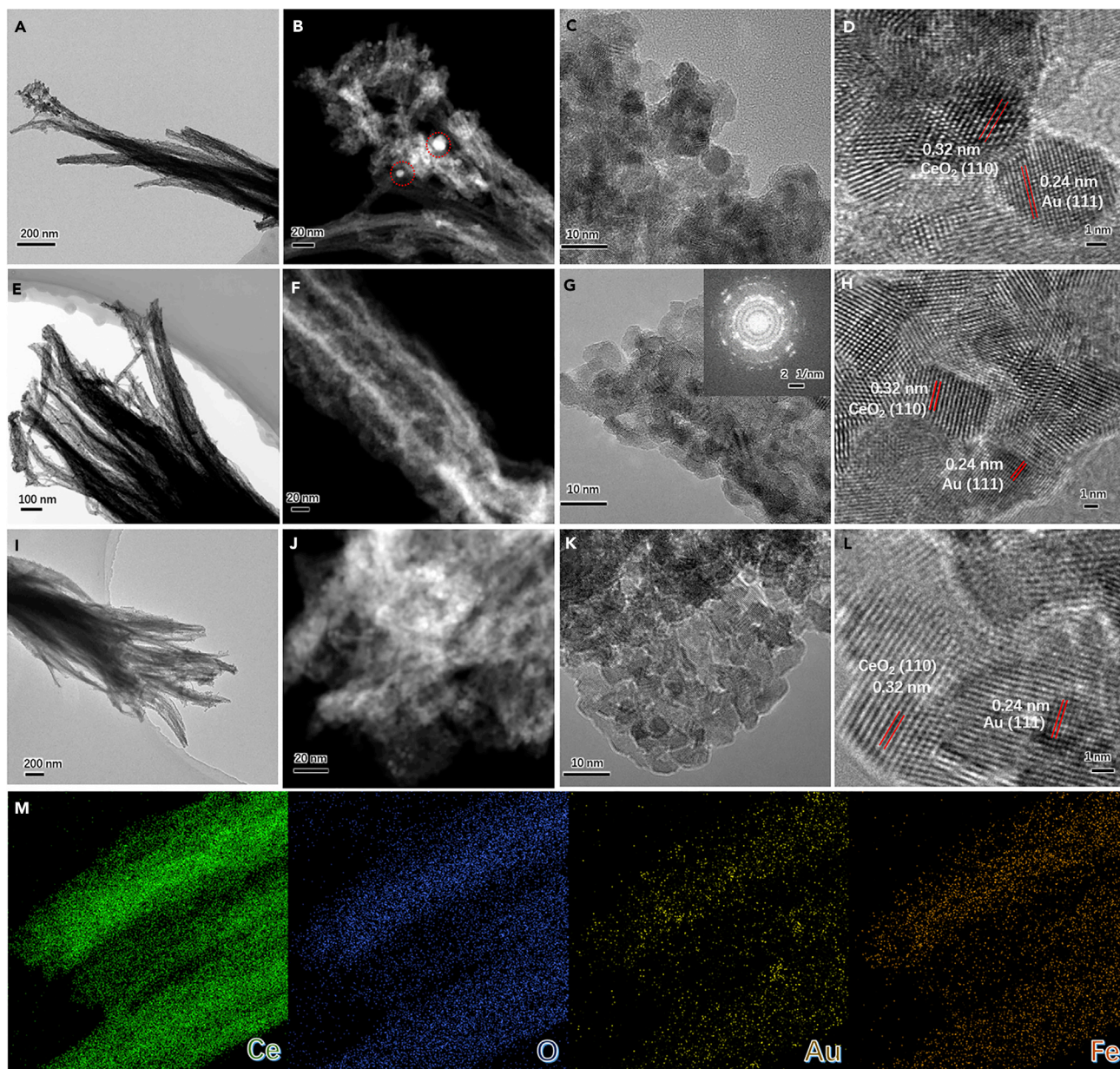


Figure 2. Morphological Characterizations, Including TEM Images, HAADF-STEM Images, High-Resolution TEM Images, and Energy-Dispersive X-Ray Spectroscopic Elemental Maps

(A–M) (A–D) Au/CeO₂, (E–H and M) hemin-Au/CeO₂, and (I–L) FePc-Au/CeO₂ catalysts. Inset in (G) shows the corresponding selected area electron diffraction (SAED) pattern. The SAED patterns of Au/CeO₂ and FePc-Au/CeO₂ samples can be found in [Figure S6](#) in the [Supplemental Information](#).

confirming the successful loading of hemin on the catalysts. The XPS spectra in Ce 3d region contain both Ce³⁺ and Ce⁴⁺ oxidation species ([Figure 3B](#)) ([Zabitskiy et al., 2015](#)). For instance, the six peaks marked as v, v', and v''' (3d_{5/2}, 882.5, 888.7, and 898.2 eV, respectively) and u, u' and u''' (3d_{3/2}, 900.1, 907.7, and 916.7 eV, respectively) were attributed to three doublets of spin-orbits of Ce⁴⁺ species ([Dutov et al., 2018](#)). And the other two peaks labeled as v' and u' (885.2 and 903.5 eV) were belonging to Ce³⁺ species. The amounts of surface Ce³⁺ in hemin-Au/CeO₂, hemin/CeO₂, and Au/CeO₂ samples were 19.3%, 21%, 20%, respectively, which was slightly higher than that of pure CeO₂ (18.8%). In addition, the Ce 3d peaks in these catalysts slightly shifted to lower B.E., indicating that the electron cloud density around the Ce increased due to the strong interaction between the guest (Au, hemin) and CeO₂ ([Jiang et al., 2015](#)). As displayed in

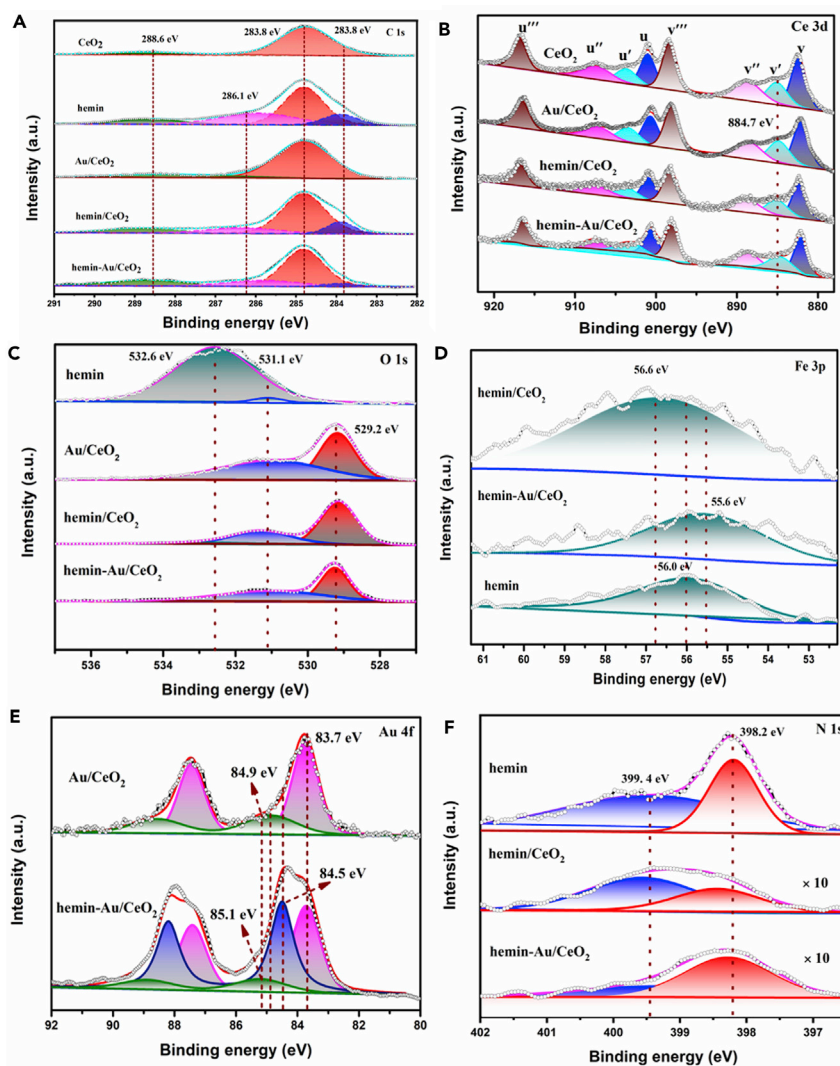


Figure 3. High-Resolution XPS Spectra of the Catalyst Samples

(A) C 1s region, (B) Ce 3d region, (C) O 1s region, (D) Fe 3p region, (E) Au 4f region, and (F) N 1s region.

Figure 3C, the corresponding XPS spectra in O 1s region can be deconvoluted into lattice oxygen at 529.2 eV and defect oxide (due to oxygen vacancies) at 531.1 eV, which indicated that enriched oxygen vacancies in the CeO₂ were produced from the Ce-BTC templated method. Both the exposed Ce³⁺ ions and enriched oxygen vacancies may promote the CO oxidation reaction (vide infra) (Ta et al., 2012).

As the Fe 2p levels were strongly overlapped with Ce Auger transitions (Figure S7 and Supplemental Information), thus the XPS spectra in the Fe 3p region with higher accuracy were analyzed. As shown in Figure 3D, there is a strong peak at around 56.0 eV being ascribed to Fe atoms in the pure hemin, which shifts to higher B.E. for hemin/CeO₂ but to lower B.E. for hemin-Au/CeO₂. It indicates that hemin was chemically bonded to the substrate, which donated electrons to the CeO₂ substrate in the absence of Au, whereas received electrons in the presence of Au. The XPS spectra in the Au 4f region were displayed in Figure 3E. It is clearly seen that Au⁰ (83.7 eV, 71.1%) is the major species in Au/CeO₂ with a minor amount of Au⁺ (84.9 eV, 28.9%). After the addition of hemin, a new peak located at 84.5 eV related to Au^{δ+} (δ < 1) was found in hemin-Au/CeO₂. More quantitatively, the Au⁺ shifted by around 0.2 eV toward higher B.E. after loading hemin. The formation of Au^{δ+} species and peak shift of Au⁺ may be due to the electron donation from Au to the empty orbitals of the Ce and Fe ions (Ha et al., 2018). Similarly, after loading FePc on Au/CeO₂, the amount of Au⁰ species decreased to 32% from 71.1% (Figure S8A and Supplemental

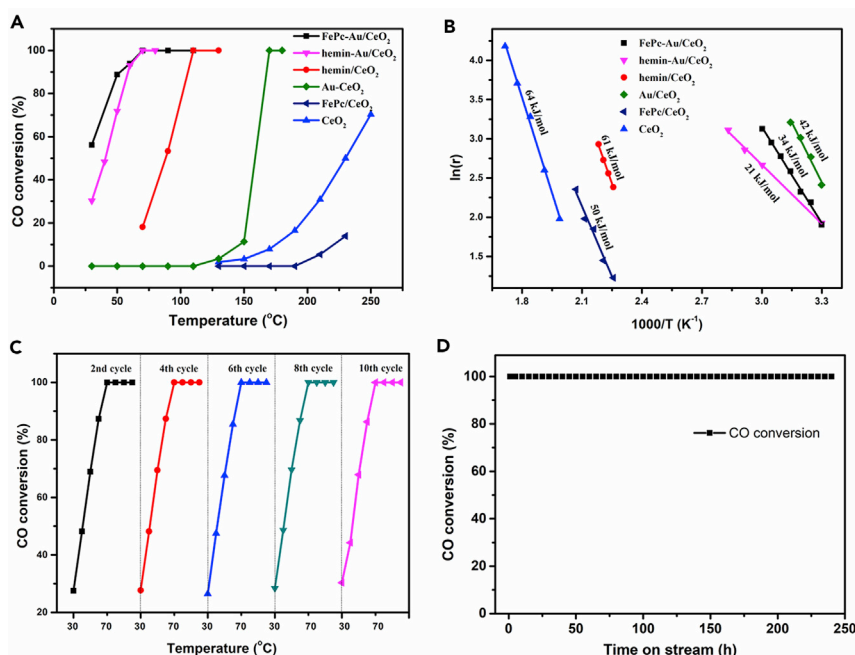


Figure 4. Catalytic Performance of Biomimetic Catalysts and Control Catalysts

(A) Temperature-dependent CO conversion data, (B) Arrhenius plots for CO oxidation, (C) CO oxidation over hemin-Au/CeO₂ catalyst tested from 30°C to 100°C with 10 consecutive recycles, and (D) CO oxidation over hemin-Au/CeO₂ catalyst maintained at 80°C for 240 h.

Information). No signal for nitrogen was detected for CeO₂ and Au/CeO₂; however, two predominant peaks with B.E. of 398.2 and 399.4 eV were observed for hemin-loaded samples (Figure 3F), corresponding to C-N=C and N-Fe, respectively (Cao et al., 2018). Likewise, the N 1s XPS analysis of the FePc-Au/CeO₂ catalyst showed the same information (Figure S8B and Supplemental Information).

CO Catalytic Oxidation Performance

The catalytic CO oxidation performance of the designed biomimetic catalysts together with the conventional catalysts was evaluated with partial pressures of CO and O₂ of 0.01 and 0.04 bar, respectively. The temperature at which the CO conversion reaching 100% is defined as T₁₀₀. As shown in Figure 4A, the pure CeO₂ exhibited inferior activity even at high temperatures (70% conversion at 250°C). Even after loading Au nanoparticles, the T₁₀₀ of Au/CeO₂ was 170°C. Interestingly, the values of T₁₀₀ were greatly decreased to 70°C, 70°C, and 110°C for hemin-Au/CeO₂, FePc-Au/CeO₂, and hemin/CeO₂, respectively. Remarkably, CO oxidation started at room temperature in the presence of hemin-Au/CeO₂ and FePc-Au/CeO₂ catalysts. When compared with other reported Au-based catalysts, our prepared biomimetic catalysts also showed superior performance to many other catalysts with lower T₁₀₀ under high gas hourly space velocity (Table S1). At the reaction temperature of 110°C, the experimental turnover frequency (TOF) of the hemin-Au/CeO₂ catalyst was 30 times greater than that of Au/CeO₂. Besides, the Arrhenius plots were used to analyze the activation energies (E_a) of different catalysts. It is worth mentioning that the reactant flow rate was adjusted to 30 mL/min to ensure that the conversion was less than 30% as measuring E_a. As shown in Figure 4B, the E_a increased in the following trend: hemin-Au/CeO₂ (21 kJ/mol) < FePc-Au/CeO₂ (34 kJ/mol) < Au/CeO₂ (42 kJ/mol) < hemin/CeO₂ (61 kJ/mol) < CeO₂ (64 kJ/mol). Therefore, the reaction pathways on hemin-Au/CeO₂ and FePc-Au/CeO₂ for CO oxidation were speculated to be different from that on other catalysts (Wang et al., 2017). As a result, it is inferred that a strong synergistic effect between Au and biomolecules contributed to the catalytic CO oxidation. We also evaluated the long-term stability of CO oxidation over the designed biomimetic catalysts (Figure 4C), which showed that the catalytic activities of hemin-Au/CeO₂ were distinctively stable in 10 consecutive recycling experiments (30°C–100°C). In addition, 100% CO conversion over the biomimetic catalyst was maintained for the long-term evaluation at 80°C for 240 h (Figure 4D). As expected, the spent hemin-Au/CeO₂ also showed

the Soret band (Figure 1E), indicating good thermostability of hemin in the CO catalytic oxidation reaction. Furthermore, as shown in Figure S9 (Supplemental Information), the organic function groups in hemin or FePc were still present in the spent catalysts. The relative amounts of gold species in the spent catalysts after evaluation for 240 h were only slightly changed with $\text{Au}^0/\text{Au}^{\delta+}/\text{Au}^+$ of 52%/41%/7% (Figure S10 and Supplemental Information). SEM and TEM images of the spent catalysts are shown in Figures S11 and S12 (Supplemental Information), indicating no obvious changes in the size and morphology of the catalysts after the long-term CO oxidation reaction. The average size of the supported Au nanoparticles was measured to be around 3 nm in both cases, which is similar to fresh catalysts. Besides, the contents of the biomolecules (Hemin or FePc) in the spent hemin-Au/CeO₂ and FePc-Au/CeO₂ catalysts were 1.86 and 2.03 wt %, respectively, suggesting good stability of the biomolecules.

Operando DRIFTS Study

To explore the promotion effects of biomolecules on CO oxidation, comparative DRIFTS data were studied by loading 10 mg of each catalyst in the DRIFTS cell with the same packing density. Under CO alone condition (the absence of reaction), DRIFTS spectra were obtained by N₂ flushing for 20 min after the saturated CO adsorption to remove the gaseous and physisorbed CO. As can be seen in Figure 5A, the adsorption of CO at 30°C was rather weak on bare CeO₂ and Au/CeO₂ with decreased intensity during N₂ flushing, which almost disappeared after continuous flushing for 20 min. As expected, obvious adsorption of CO was found in the biomolecules (pure hemin or FePc). Interestingly, the co-loading of Au and biomolecules on CeO₂ led to significantly enhanced adsorption strength of CO species over the biometric catalysts, which was nearly 70-fold over that on pure biomolecules. Two major bands (at 2,117 and 2,170 cm⁻¹) can be tentatively attributed to two types of carbonyl stretching vibrations (El-Bahy et al., 2011; Luo et al., 2017). The conclusion is supported by the CO pulse chemisorption test, which indicated that the amounts of CO adsorption were 212.5, 247.5, 120, 28, and 5.35 μmol/g for hemin-Au/CeO₂, FePc-Au/CeO₂, hemin/CeO₂, Au/CeO₂, CeO₂, respectively. Interestingly, the value of CO uptake from hemin-Au/CeO₂ was higher than the sum of uptake from the two mono-guest catalysts (hemin/CeO₂ + Au/CeO₂), further confirming the synergy between Au and biomolecules for CO adsorption. Based on an operando DRIFTS study (Chen et al., 2015), Huang et al. reported that within the studied sizes (in the range of 2–6 nm) of supported Au nanoparticles on CeO₂, the size of Au nanoparticles did not affect the intrinsic oxidation reactivity of CO_{ad}. Thus, the varied activities of different catalysts were ascribed to the specific density of surface CO_{ad}. Combined with the size data of Au in our prepared catalysts, herein, the large difference in the CO pulse chemisorption data was unlikely due to the different sizes of Au (based on the dispersion [D]), but it should be due to the presence of biomolecules. Therefore, we believe that the cooperative effect between hemin (or FePc) and Au nanoparticles of the biomimetic catalysts was the major reason for the superior CO oxidation performance.

We then studied the CO oxidation progress by O₂ purge over the adsorbed CO. As shown in Figures 5B and 5C, after 14 s of contact with O₂ at 30°C, the adsorbed CO signals over hemin-Au/CeO₂ and FePc-Au/CeO₂ were strongly attenuated with the appearance of two new bands at around 2,345 and 2,362 cm⁻¹, which can be ascribed to a doublet of gaseous CO₂ (Jones et al., 2016), suggesting a good catalytic activity. These results are consistent with the catalytic evaluations, which suggest a good CO conversion efficiency at low temperatures (e.g., 30°C). In contrast, in the case of pure hemin and FePc, it was found that CO adsorbed firmly on hemin, which failed to achieve conversion even 1,200 s after O₂ continuous purging (Figures 5D and 5E). As previously mentioned, the strong CO adsorption during oxidation would cause the poison of CO, which must desorb before the oxidation reaction can proceed. Also, the oxygen cannot be activated on hemin and FePc; consequently, it sounds reasonable that biomolecules alone have a poor activity to convert CO to CO₂ unless they were supported on CeO₂. In the case of Au/CeO₂ shown in Figure S13 (Supplemental Information), 600 s after O₂ continuous purging, the CO was fully oxidized as CO₂ and no adsorbed CO remained. Moreover, temperature-dependent DRIFTS of oxidation of CO adsorbed on pure hemin was studied in Figure 5F. Clearly, with increasing temperature, the peak intensities of hemin-CO were gradually weakened with the increase of temperature (30°C–110°C) and disappear at 130°C. It means that the oxidation of CO on hemin requires a high reaction temperature.

DFT Calculation Results

Depending on the cluster structure and carrier type, numerous works have been dedicated to the reaction mechanisms of CO oxidation through both theoretical and experimental studies. It is crucial to build an appropriate DFT computational model that mimics the realistic catalysts in experiments. Herein, Au

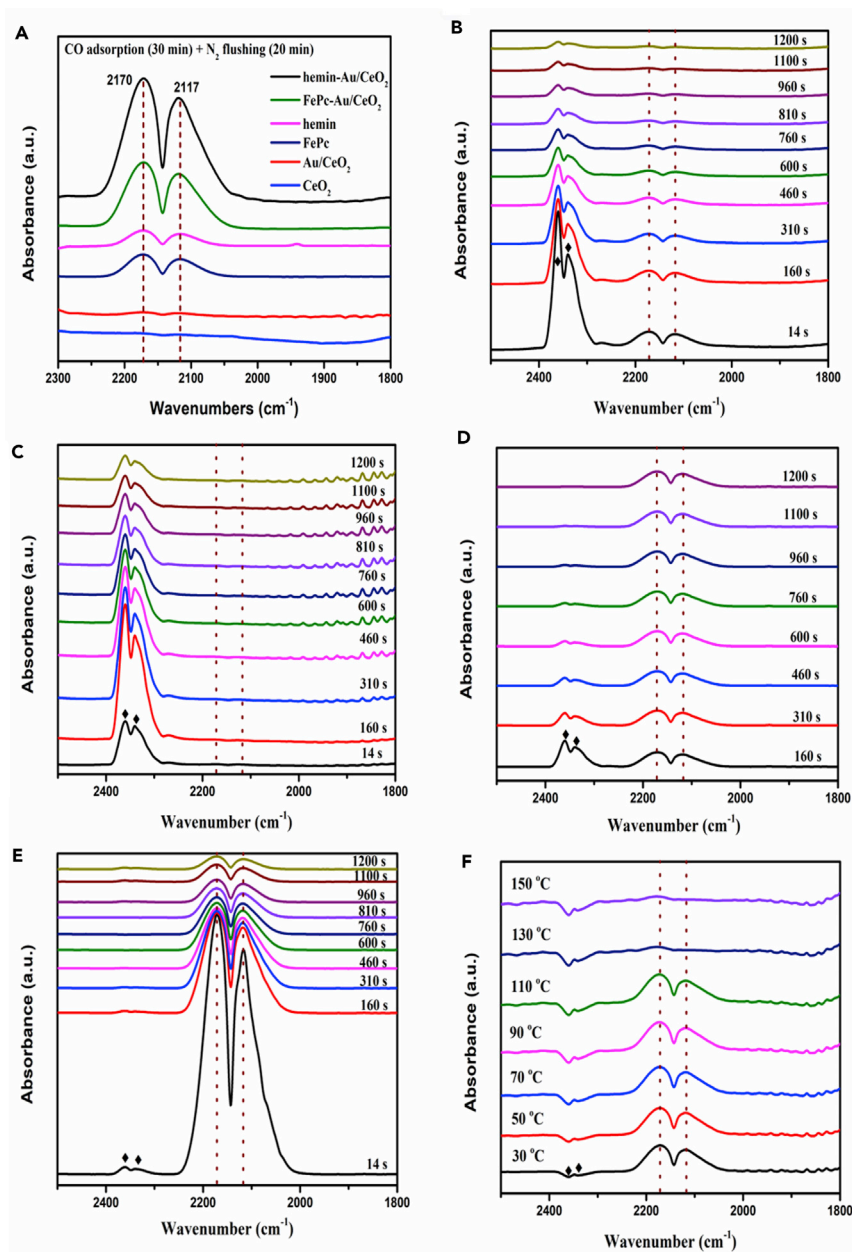


Figure 5. Operando DRIFTS Results

(A) Infrared (IR) spectra of CO adsorption over different samples after N₂ flushing for 20 min at 30°C. (B–F) Time-dependent IR spectra during the oxidation process over (B) hemin-Au/CeO₂, (C) FePc-Au/CeO₂, (D) pure hemin, and (E) pure FePc at 30°C via continuous O₂ purging, and (F) temperature-dependent IR spectra of CO adsorbed on hemin when exposing to O₂ flow.

possesses a characteristic electronic structure with a contracted 6s shell and a significant s-d hybridization, and the Au₁₃ with a sufficiently stable structure was then chosen for optimization (Kim et al., 2012). Based on the previous work by Kim et al. (2012), defect-free CeO₂ (111) 3 × 3 × 2 slab model was applied as the substrate for study on the interaction of Au and basement. A simplified hemin model comprising a five-coordinated Fe was used to explore the important role of biomolecules in our catalysts. Then, representative Au/CeO₂(111) and hemin/Au/CeO₂(111) models were constructed to investigate the charge transfer and interfacial interactions among hemin, Au₁₃, and CeO₂ substrate (Ha et al., 2018).

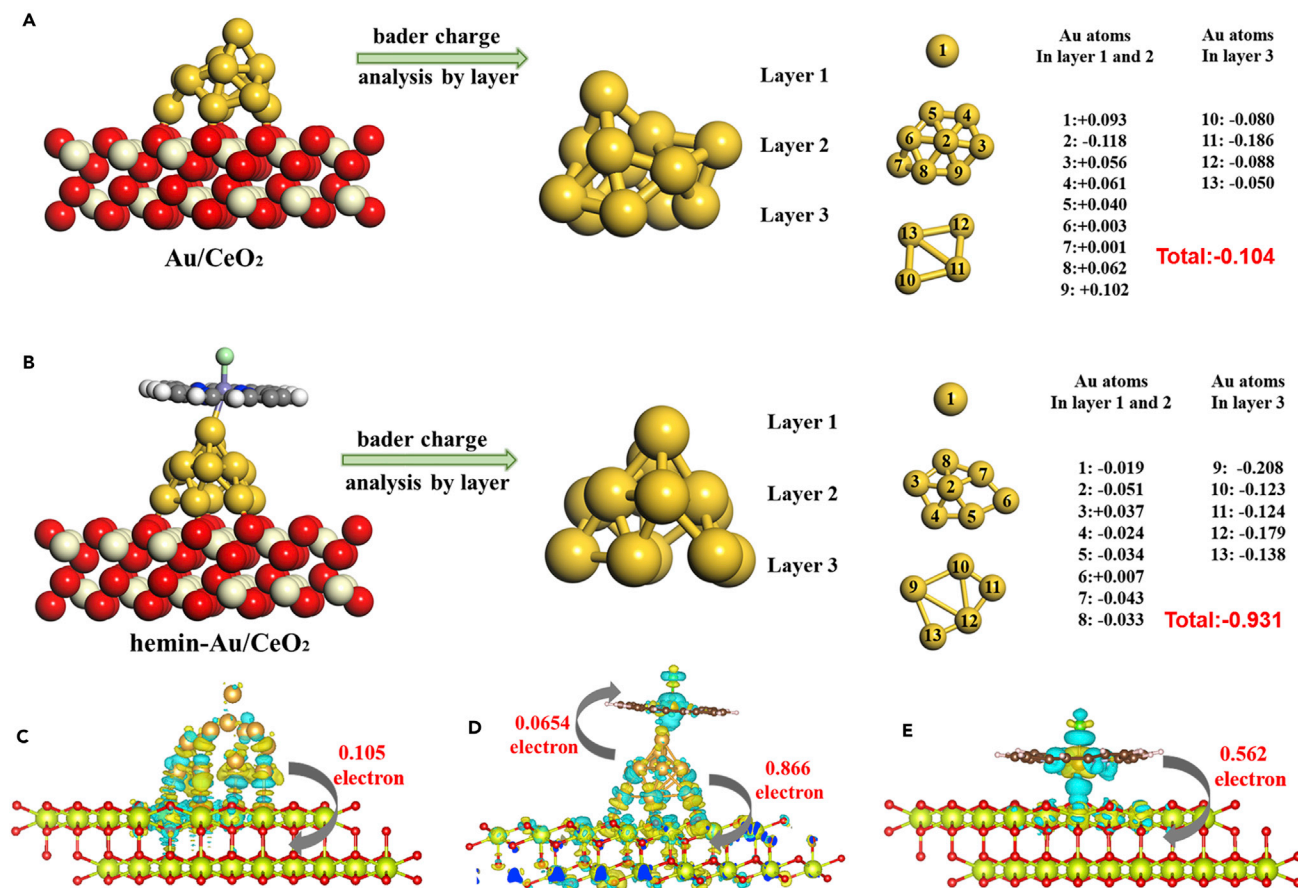


Figure 6. Electronic Interactions among the Different Components in Catalysts

(A) Bader electron summary of Au/CeO₂, (B) Bader electron summary of hemin-Au/CeO₂, (C) Bader charge difference result of Au/CeO₂, (D) Bader charge difference result of hemin-Au/CeO₂, and (E) Bader charge difference result of hemin/CeO₂.

Electronic Interactions among the Multicomponent Hemin-Au/CeO₂

As shown in Scheme 1B, Au₁₃ in Au/CeO₂ and hemin-Au/CeO₂ were loaded on CeO₂ substrate through a gold-oxygen bond. Different from the isolated Au₁₃, the empty 4f-orbital localized on Ce⁴⁺ ions of CeO₂ attracted electrons from Au₁₃ through an oxygen bridge, resulting in a change in the valence electron configuration of Au₁₃. The balance of the s-d hybridization of Au was broken and induced the structural evolution of Au₁₃. As displayed in Figures 6A and 6B, we further analyzed the Au atoms layer by layer. For instance, Au₁₃ in hemin-Au/CeO₂ system consists of the first layer (Au-1), the second layer (Au2-Au8), and the third layer (Au9-Au13), wherein Au-3 and Au-11 were recognized as the active perimeter sites. Interestingly, the Au₁₃ bonded the CeO₂(111) substrate through four Au atoms in Au/CeO₂ but five atoms in hemin-Au/CeO₂. It was inferred that the existence of hemin can restructure the interfacial perimeters and strengthen the interfacial interaction of Au-CeO₂, wherein, the Au₁₃ structure was transformed from the original unstable mountain shape to a relatively stable hemisphere shape. With the enhanced interaction, Au nanoparticles could only rotate/vibrate locally but could not migrate to form aggregates. Bader charge calculation was further performed to analyze the electronic interaction between Au and CeO₂ in both samples. As shown in Figures 6C and 6D, in Au/CeO₂, positively charged Au donated 0.105 electron to the empty 4f-band of CeO₂, whereas, surprisingly, a remarkable charge transfer (0.866 e) from Au to ceria was found in hemin-Au/CeO₂, reflecting a strong interfacial anchoring effect. Hemin gained 0.0654 electron from the first layer (Au-1) in Au₁₃ through N bridge, which thereby weakened the Au-Au bond with the second layer and enhanced the Au-CeO₂ interaction by forming strong covalent bonds with oxygen atoms in the catalyst support (Ta et al., 2012). The restructuring of the active Au-CeO₂ interface indicates that hemin played an important role in Au structural evolution, which may be the reason that a decreased

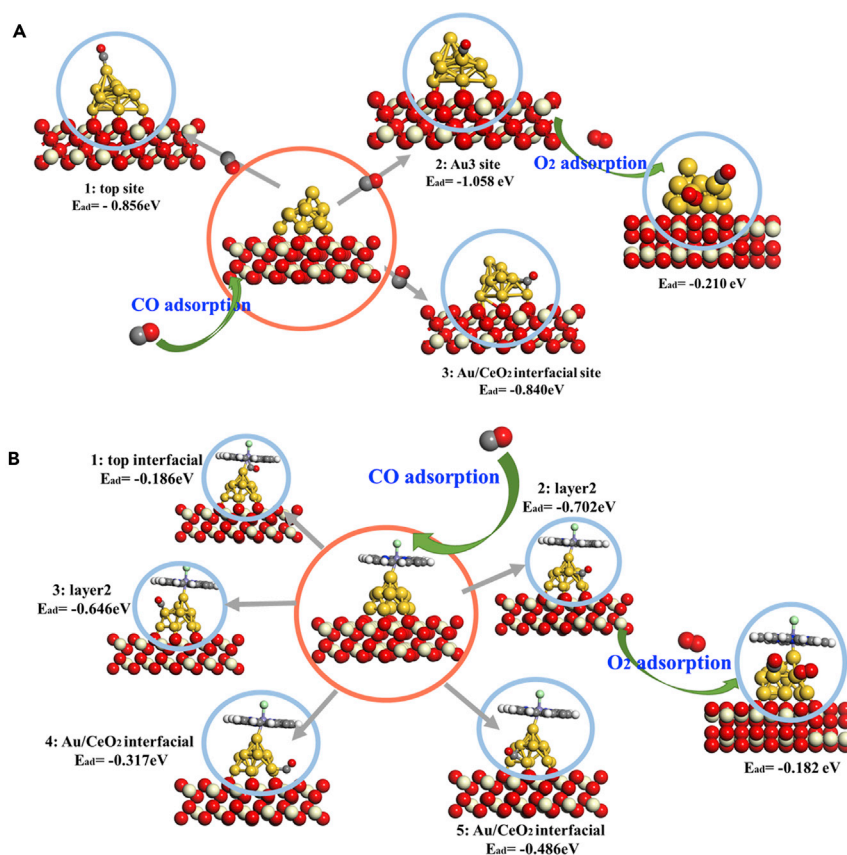


Figure 7. Schematic Illustrations of the Various CO Adsorption Sites and Co-adsorbed O₂ on the Catalysts
(A) Au/CeO₂ and (B) hemin-Au/CeO₂.

particle size was experimentally observed in hemin-Au/CeO₂, compared with Au/CeO₂ (2.5 nm versus 5.6 nm). It should be noted that the positively charged Au were mainly localized in the bottom layer of Au atoms contacting with CeO₂. As shown in Figure 6E, the hemin would donate 0.562 electron to CeO₂ substrate via Fe-O coordination if it was directly loaded on the metal oxide substrate. The structure of the FePc molecule on the top position of Au/CeO₂ was also optimized, and the electronic interactions among FePc, Au₁₃, and CeO₂ were calculated. According to Figure S14 (Supplemental Information), the FePc molecule donated 0.532 electrons to Au because the central Fe atom was four-coordinated. Meanwhile, the Au donated 0.590 electron to the empty 4f-band of CeO₂. Bader charge calculation results indicate that the interaction between Au and CeO₂ in FePc-Au/CeO₂ was relatively stronger compared with Au/CeO₂.

Langmuir-Hinshelwood Mechanism

As above mentioned, there is optimum bonding strength between metal and CO for screening eligible catalysts for CO oxidation according to the Sabatier principle, neither too strong nor too weak. In the Langmuir-Hinshelwood mechanism, CO oxidation is expected to undergo co-adsorption of CO and O₂ on Au₁₃, and strong adsorption of CO always leads to large reaction barriers. Modifying Au nanoparticles with alloying elements (Ag, Cu, or Al) was considered to be a good way to reduce CO adsorption (Li et al., 2013). To explore the modification effect of hemin on Au nanoparticles, we simulated several adsorption sites of CO on Au-CeO₂ from the top of the gold cluster (layer 1) to the interface (layer 3).

As shown in Figure 7A, the low-coordinated Au corner site (Au-3) adsorbed CO strongly (E_{ad} of -1.05 eV) in the case of Au/CeO₂, and the interfacial site showed a relatively weak adsorption (-0.84 eV), even though CO bound with two Au atoms. However, for hemin-Au/CeO₂ (Figure 7B), CO was preferential adsorbed on the second layer on Au₁₃ (Au-6) with E_{ad} of -0.7 eV, which was 0.305 eV larger than Au/CeO₂, indicating

weaker adsorption. A negative E_{ad} value indicates that the adsorption of CO gas molecules on the Au surface is energetically favorable. Besides, C-O bond lengths for free CO, CO adsorbed on hemin-Au/CeO₂, and CO adsorbed on Au/CeO₂ were 1.143, 1.144, and 1.159 Å, respectively, which was closely related to the valence and configuration of Au₁₃. According to the frontier orbital theory, the highest occupied molecular orbital (5σ) was a non-bonding orbital in the free CO molecules (Camellone and Fabris, 2009). Therefore, its hybridization with metal atoms did not affect the strength of the C-O bond. However, the lowest unoccupied molecular orbital ($2\pi^*$) was an anti-bonding orbital. When CO adsorbed on Au, the back-donation of electrons from Au would partially fill the $2\pi^*$ orbital, thereby, the C-O bond became weakened and the adsorption was strengthened. As discussed before, hemin strengthened the interaction of Au₁₃-CeO₂, and most of the Au on the surface of Au₁₃ were positively charged. Accordingly, the more electrons Au loses, the weaker is its ability to fill $2\pi^*$ orbital in CO. Besides, as shown in Figure S15 (Supplemental Information), the Au in hemin/Au/CeO₂ exhibits a d -band center at -3.27 eV, whereas it shifts to -3.14 eV in Au/CeO₂. From a quantum chemical view, a deeper d -band center indicates a weak ability for back-donation of electrons, being consistent with the tendency of adsorption energy. Different from the five-coordinated Fe in hemin molecule, which can break the balance of the s - d hybridization of Au and induce the structural evolution of Au₁₃, in the case of FePc molecule, the four-coordinated Fe played the role of electron compensation to Au. Besides, it was found that CO preferentially adsorbed on the second layer on Au₁₃ with E_{ad} of -0.948 eV, which was 0.110 eV larger than that of Au/CeO₂ (Figure S14C and Supplemental Information). It was noticeable that the E_{ad} of O₂ on the catalyst surface (in the presence of adsorbed CO) increased to -0.447 eV on FePc-Au/CeO₂ compared with two other models (-0.210 eV for Au/CeO₂ and -0.182 eV for hemin-Au/CeO₂). The weaker CO adsorption and stronger oxygen adsorption would reduce the reaction energy barrier of CO oxidation. However, FePc itself can serve as an adsorption site of CO with E_{ad} of -1.341 eV (Figure S14D and Supplemental Information), which significantly affects the catalytic activity of FePc-Au/CeO₂. The calculated results are consistent with the experimental results.

We also took the adsorption of CO on hemin into consideration. As shown in Figure S16 (Supplemental Information), the presence of iron centers in hemin allows to moderately adsorb CO ($E_{\text{ad}} = -0.468$ eV) via the $3d$ levels hybridized with CO valence state (Wu et al., 2019; Zhang et al., 2018). To explore the competitive adsorption of CO and O₂ on hemin, we then built the co-adsorption model, and the result showed that highly coordinated Fe could only adsorb CO and would expel O₂. Instead of being a reaction site, hemin can play a beneficial role in transporting CO to the metal or the basement and promote the oxidation process. Meanwhile, the adsorption energy of O₂ on the catalyst surface (in the presence of adsorbed CO) did not change much with or without the hemin (i.e., -0.210 eV for Au/CeO₂ and -0.182 eV for hemin-Au/CeO₂).

Mars-van Krevelen Mechanism

The Mars-van Krevelen (M-vK) mechanism is another mechanism of CO oxidation featured with CO oxidation via nearby lattice oxygen in the substrate and O vacancy replenishing process (Kim et al., 2012). A low oxygen vacancy formation energy (E_{vac}) facilitates the CO oxidation mechanism at the Au-CeO₂ interface. As shown in Figures 8A and 8B, with the decoration of hemin on Au nanoparticles, the E_{vac} values of CeO₂ decreased from 2.588 eV (Au/CeO₂) to 2.413 eV (hemin-Au/CeO₂). Combining the above Bader charge data, hemin molecules promoted the formation of stronger Au-CeO₂ electronic interactions, which facilitated the reduction of Ce⁴⁺ to Ce³⁺. Acting as an electron reservoir, the more positively charged Au atoms on CeO₂ can absorb the electrons released when oxygen vacancies are formed. Our calculation results are consistent with the previous work (Schlexer et al., 2018), confirming that Au^{δ+} facilitates the formation of more amount of oxygen vacancy. Then, during the vacancy healing step (i.e., replenishing the vacancies by reaction with O₂), the O₂ molecule can strongly bond to the oxygen vacancy with very negative adsorption energy (-2.53 eV for Au/CeO₂ and -2.58 eV for hemin-Au/CeO₂, Figure S17 and Supplemental Information). Accordant with the previous work (Schlexer et al., 2018), our calculation results proved that the oxygen healing step of hemin-Au-CeO₂ was highly efficient. Furthermore, we also calculated E_{vac} when directly loading hemin on CeO₂ support. As shown in Figure 8C, the five-coordinated Fe in hemin donated electrons to CeO₂ through an oxygen bridge, and oxygen was slightly pulled away from the surface. Bader charge result showed that hemin donated 0.56 electron to CeO₂ and the electrons were localized on the four Ce atoms around the oxygen bridge. The E_{vac} on hemin/CeO₂ was 1.98 eV, which was 0.608 eV lower than the Au/CeO₂. Therefore, it can be safely concluded that the high coordination of Fe in hemin can greatly promote the formation of oxygen vacancies and improve the activity of the catalyst for CO oxidation.

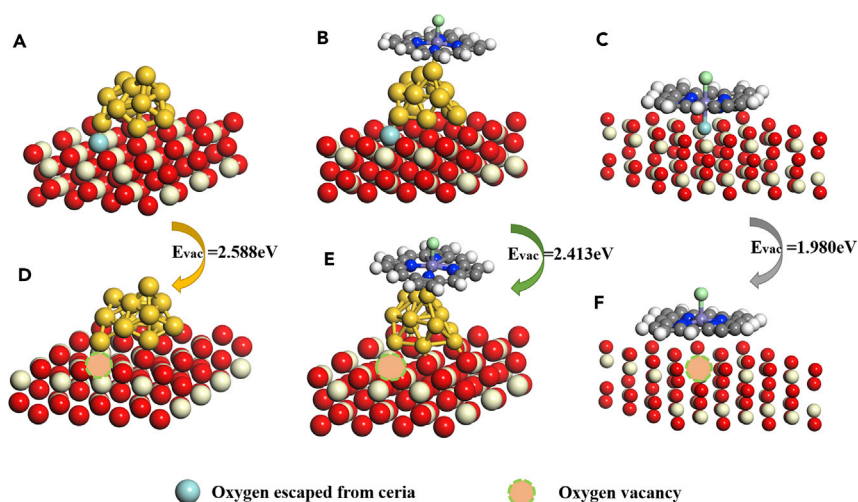


Figure 8. Comparison of the Oxygen Vacancy Formation Energy over the Different Catalysts

Optimized structure models of (A) Au₁₃ cluster loaded on CeO₂ support (Au/CeO₂), (B) hemin loaded on the top site of Au/CeO₂ (hemin-Au/CeO₂), and (C) hemin loaded on CeO₂ support (hemin/CeO₂).

The illustrations of the formation of individual oxygen vacancy due to oxygen escaping from ceria in the cases of (D) Au/CeO₂, (E) hemin-Au/CeO₂, and (F) hemin/CeO₂.

Conclusion

We have prepared a series of biomimetic catalysts by loading biomolecules (hemin or its analog FePc) on Au/CeO₂, wherein, hemin could be anchored on the support through covalent bonds. The electronic interactions between biomolecules, Au, and ceria were experimentally and theoretically discussed, which suggests that the released electrons from Au nanoparticles were localized to the empty 4f-band of the CeO₂ substrate, and hemin also gained 0.0654 electrons from the first layer (Au-1) in Au₁₃. Compared with the Au-CeO₂ interface, the positively charged Au in the presence of hemin provides the anchoring sites for both CO and O₂ in the case of the Langmuir-Hinshelwood mechanism. The synergistic effects were observed between the dual active sites (Au and biomolecules) in CO oxidation, which was started at room temperature in the presence of hemin-Au/CeO₂ and FePc-Au/CeO₂ catalysts. The experimental turnover frequency of the hemin-Au/CeO₂ catalyst was 30 times greater than that of Au/CeO₂ at a reaction temperature of 110°C. According to the characterizations and catalytic mechanisms analysis, there are multiple factors jointly contributing to the unexpected CO oxidation reactivity over biomimetic catalysts, including (1) relatively lower adsorption energy of CO and strong adsorption of O₂, (2) the electronic interactions of the guest (biomolecule or Au) and substrate promote the formation of Ce³⁺ and oxygen vacancy in ceria support (in the case of M-vK mechanism), (3) local synergistic effects between Au and biomolecule sites, and (4) stabilization of Au nanoparticles on ceria via restructuring of the Au-CeO₂ interface periphery. Taking together, our rapid and cheap synthetic protocol yields promising biomimetic catalysts with superior CO oxidation reactivity and stability, which paves the way to the use of other catalytically active biomolecules as heterogeneous catalysts.

Limitations of the Study

This work provides insights on how to develop biomimetic catalysts by the integration of biomolecules (hemin or ferrous phthalocyanine) onto well-defined Au/CeO₂, which eventually leads to the improved catalytic performance in CO oxidation at low temperatures. Future work is required to analyze other types of biomolecules and extend the method to functionalize other conventional catalysts.

Resource Availability

Lead Contact

Further information and requests for resources and reagents should be directed to and will be fulfilled by the Lead Contact, Guowu Zhan (gwzhan@hqu.edu.cn).

Materials Availability

This study did not generate new unique reagents.

Data and Code Availability

The data that support the findings of this study are available from the corresponding author upon reasonable request.

METHODS

All methods can be found in the accompanying [Transparent Methods supplemental file](#).

SUPPLEMENTAL INFORMATION

Supplemental Information can be found online at <https://doi.org/10.1016/j.isci.2020.101852>.

ACKNOWLEDGMENTS

This work was financially supported by the National Natural Science Foundation of China (Nos. 21908073 & 21536010), the Natural Science Foundation of Fujian Province (Nos. 2019J01074 & 2019J01075), and Post-graduates' Innovative Fund in Scientific Research of Huaqiao University. We also thank the Analysis and Testing Center of Huaqiao University for providing part of the characterizations.

AUTHOR CONTRIBUTIONS

L.F.: Conceptualization, Investigation, and Writing – Original Draft. J.D.: Conceptualization, Investigation, and Review & Editing. Z.H.: Investigation. J.X.: Writing – Review & Editing. Q.L.: Methodology. J.H.: Writing and Conceptualization. S.-F.Z.: Writing and Conceptualization. G.Z.: Writing – Review & Editing, Supervision, and Conceptualization.

DECLARATION OF INTERESTS

The authors declare no competing interests.

Received: September 3, 2020

Revised: October 28, 2020

Accepted: November 18, 2020

Published: December 18, 2020

REFERENCES

- Alayoglu, S., Nilekar, A.U., Mavrikakis, M., and Eichhorn, B. (2008). Ru-Pt core-shell nanoparticles for preferential oxidation of carbon monoxide in hydrogen. *Nat. Mater.* **7**, 333–338.
- Allian, A.D., Takanabe, K., Fujidala, K.L., Hao, X., Truex, T.J., Cai, J., Buda, C., Neurock, M., and Iglesia, E. (2011). Chemisorption of CO and mechanism of CO oxidation on supported platinum nanoclusters. *J. Am. Chem. Soc.* **133**, 4498–4517.
- Breslow, R. (1995). Biomimetic chemistry and artificial enzymes: catalysis by design. *Acc. Chem. Res.* **28**, 146–153.
- Camellone, M.F., and Fabris, S. (2009). Reaction mechanisms for the CO oxidation on Au/CeO₂ catalysts: activity of substitutional Au³⁺/Au⁺ cations and deactivation of supported Au⁺ adatoms. *J. Am. Chem. Soc.* **131**, 10473–10483.
- Cao, Y., Si, W., Hao, Q., Li, Z., Lei, W., Xia, X., Li, J., Wang, F., and Liu, Y. (2018). One-pot fabrication of Hemin-NC composite with enhanced electrocatalysis and application to H₂O₂ sensing. *Electrochim. Acta* **261**, 206–213.
- Chen, S., Luo, L., Jiang, Z., and Huang, W. (2015). Size-dependent reaction pathways of low-temperature CO oxidation on Au/CeO₂ catalysts. *ACS Catal.* **5**, 1653–1662.
- Chen, Y.Z., Gu, B., Uchida, T., Liu, J., Liu, X., Ye, B.J., Xu, Q., and Jiang, H.L. (2019). Location determination of metal nanoparticles relative to a metal-organic framework. *Nat. Commun.* **10**, 3462.
- Decréau, R.A., Collman, J.P., and Hosseini, A. (2010). Electrochemical applications. How click chemistry brought biomimetic models to the next level: electrocatalysis under controlled rate of electron transfer. *Chem. Soc. Rev.* **39**, 1291–1301.
- Dutov, V.V., Mamontov, G.V., Zaikovskii, V.I., Liotta, L.F., and Vodyankina, O.V. (2018). Low-temperature CO oxidation over Ag/SiO₂ catalysts: effect of OH/Ag ratio. *Appl. Catal. B* **221**, 598–609.
- El-Bahy, Z.M., Hanafy, A.I., Ibrahim, M.M., and Anpo, M. (2011). In situ FTIR studies of CO oxidation over Fe-free and Fe-promoted PtY catalysts: effect of water vapor addition. *J. Mol. Catal. A* **344**, 111–121.
- Fan, L., Zhao, F., Huang, Z., Chen, B., Zhou, S.-F., and Zhan, G. (2019). Partial deligandation of M/Ce-BTC nanorods (M = Au, Cu, Au-Cu) with “Quasi-MOF” structures towards improving catalytic activity and stability. *Appl. Catal. A* **572**, 34–43.
- Gu, Z.-Y., Park, J., Raiff, A., Wei, Z., and Zhou, H.-C. (2014). Metal-organic frameworks as biomimetic catalysts. *ChemCatChem* **6**, 67–75.
- Guo, Y., Deng, L., Li, J., Guo, S., Wang, E., and Dong, S. (2011). Hemin–graphene hybrid nanosheets with intrinsic peroxidase-like activity for label-free colorimetric detection of single-nucleotide polymorphism. *ACS Nano* **5**, 1282–1290.
- Ha, H., Yoon, S., An, K., and Kim, H.Y. (2018). Catalytic CO oxidation over Au nanoparticles supported on CeO₂ nanocrystals: effect of the Au–CeO₂ interface. *ACS Catal.* **8**, 11491–11501.
- Jiang, D., Wang, W., Zhang, L., Zheng, Y., and Wang, Z. (2015). Insights into the surface-defect dependence of photoreactivity over CeO₂ nanocrystals with well-defined crystal facets. *ACS Catal.* **5**, 4851–4858.
- Jones, J., Xiong, H., DeLaRiva, A.T., Peterson, E.J., Pham, H., Challa, S.R., Qi, G., Oh, S., Wiebenga, M.H., Pereira Hernandez, X.I., et al. (2016). Thermally stable single-atom platinum-on-ceria catalysts via atom trapping. *Science* **353**, 150–154.
- Kim, H.Y., Lee, H.M., and Henkelman, G. (2012). CO oxidation mechanism on CeO₂-supported Au nanoparticles. *J. Am. Chem. Soc.* **134**, 1560–1570.

- Lee, Y., He, G., Akey, A.J., Si, R., Flytzani-Stephanopoulos, M., and Herman, I.P. (2011). Raman analysis of mode softening in nanoparticle CeO_{2-x} and Au- CeO_{2-x} during CO oxidation. *J. Am. Chem. Soc.* **133**, 12952–12955.
- Li, D., Zhu, Y., Wang, H., and Ding, Y. (2013). Nanoporous gold as an active low temperature catalyst toward CO oxidation in hydrogen-rich stream. *Sci. Rep.* **3**, 3015.
- Li, Z., Tian, B., Zhen, W., Wu, Y., and Lu, G. (2017). Inhibition of hydrogen and oxygen recombination using oxygen transfer reagent hemin chloride in Pt/TiO₂ dispersion for photocatalytic hydrogen generation. *Appl. Catal. B* **203**, 408–415.
- Lian, M., Xue, Z., Qiao, X., Liu, C., Zhang, S., Li, X., Huang, C., Song, Q., Yang, W., Chen, X., and Wang, T. (2019). Movable hollow nanoparticles as reactive oxygen scavengers. *Chem* **5**, 2378–2387.
- Liang, M., Borjigin, T., Zhang, Y., Liu, B., Liu, H., and Guo, H. (2019). Controlled assemble of hollow heterostructured g-C₃N₄@CeO₂ with rich oxygen vacancies for enhanced photocatalytic CO₂ reduction. *Appl. Catal. B* **243**, 566–575.
- Liang, Z.-X., Song, H.-Y., and Liao, S.-J. (2011). Hemin: a highly effective electrocatalyst mediating the oxygen reduction reaction. *J. Phys. Chem. C* **115**, 2604–2610.
- Luo, J., Liu, Y., Niu, Y., Jiang, Q., Huang, R., Zhang, B., and Su, D. (2017). Insight into the chemical adsorption properties of CO molecules supported on Au or Cu and hybridized Au–CuO nanoparticles. *Nanoscale* **9**, 15033–15043.
- Luo, Y.C., Chu, K.L., Shi, J.Y., Wu, D.J., Wang, X.D., Mayor, M., and Su, C.Y. (2019). Heterogenization of photochemical molecular devices: embedding a metal-organic cage into a ZIF-8-derived matrix to promote proton and electron transfer. *J. Am. Chem. Soc.* **141**, 13057–13065.
- Ma, M., Yan, Wang, J.-Y., Li, Q.-X., and Cai, W.-B. (2007). A study of NO adducts of iron protoporphyrin IX adlayer on Au electrode with in situ ATR-FTIR spectroscopy. *J. Phys. Chem. C* **111**, 8649–8654.
- Marchetti, L., and Levine, M. (2011). Biomimetic catalysis. *ACS Catal.* **1**, 1090–1118.
- Peterson, E.J., DeLaRiva, A.T., Lin, S., Johnson, R.S., Guo, H., Miller, J.T., Hun Kwak, J., Peden, C.H., Kiefer, B., Allard, L.F., et al. (2014). Low-temperature carbon monoxide oxidation catalysed by regenerable atomically dispersed palladium on alumina. *Nat. Commun.* **5**, 4885.
- Savagatrup, S., Schroeder, V., He, X., Lin, S., He, M., Yassine, O., Salama, K.N., Zhang, X.-X., and Swager, T.M. (2017). Bio-inspired carbon monoxide sensors with voltage-activated sensitivity. *Angew. Chem. Int. Ed.* **56**, 14066–14070.
- Schlexer, P., Widmann, D., Behm, R.J., and Pacchioni, G. (2018). CO oxidation on a Au/TiO₂ nanoparticle catalyst via the Au-assisted Mars–van Krevelen mechanism. *ACS Catal.* **8**, 6513–6525.
- Ta, N., Liu, J., Chenna, S., Crozier, P.A., Li, Y., Chen, A., and Shen, W. (2012). Stabilized gold nanoparticles on ceria nanorods by strong interfacial anchoring. *J. Am. Chem. Soc.* **134**, 20585–20588.
- Tan, Q., Shu, C., Abbott, J., Zhao, Q., Liu, L., Qu, T., Chen, Y., Zhu, H., Liu, Y., and Wu, G. (2019). Highly dispersed Pd–CeO₂ nanoparticles supported on N-doped core–shell structured mesoporous carbon for methanol oxidation in alkaline media. *ACS Catal.* **9**, 6362–6371.
- Tegeder, P., Freitag, M., Chepiga, K.M., Muratsugu, S., Moller, N., Lamping, S., Tada, M., Glorius, F., and Ravoo, B.J. (2018). N-heterocyclic carbene-modified Au–Pd alloy nanoparticles and their application as biomimetic and heterogeneous catalysts. *Chemistry* **24**, 18682–18688.
- Wang, L., Yang, H., He, J., Zhang, Y., Yu, J., and Song, Y. (2016). Cu–Hemin metal-organic-frameworks/chitosan-reduced graphene oxide nanocomposites with peroxidase-like bioactivity for electrochemical sensing. *Electrochim. Acta* **213**, 691–697.
- Wang, W., Cao, Z., Liu, K., Chen, J., Wang, Y., and Xie, S. (2017). Ligand-assisted, one-pot synthesis of Rh-on-Cu nanoscale sea urchins with high-density interfaces for boosting CO oxidation. *Nano Lett.* **17**, 7613–7619.
- Wang, X., Liu, D., Song, S., and Zhang, H. (2013). Pt@CeO₂ multicore@shell self-assembled nanospheres: clean synthesis, structure optimization, and catalytic applications. *J. Am. Chem. Soc.* **135**, 15864–15872.
- Wei, P.J., Yu, G.Q., Naruta, Y., and Liu, J.G. (2014). Covalent grafting of carbon nanotubes with a biomimetic heme model compound to enhance oxygen reduction reactions. *Angew. Chem. Int. Ed.* **53**, 6659–6663.
- Wu, Y., Jiang, Z., Lu, X., Liang, Y., and Wang, H. (2019). Domino electroreduction of CO₂ to methanol on a molecular catalyst. *Nature* **575**, 639–642.
- Xue, T., Jiang, S., Qu, Y., Su, Q., Cheng, R., Dubin, S., Chiu, C.Y., Kaner, R., Huang, Y., and Duan, X. (2012). Graphene-supported hemin as a highly active biomimetic oxidation catalyst. *Angew. Chem. Int. Ed.* **51**, 3822–3825.
- Yu, T., Zeng, Y., Chen, J., Li, Y.Y., Yang, G., and Li, Y. (2013). Exceptional dendrimer-based mimics of diiron hydrogenase for the photochemical production of hydrogen. *Angew. Chem. Int. Ed.* **52**, 5631–5635.
- Zabitskiy, M., Djinić, P., Tchernychova, E., Tkachenko, O.P., Kustov, L.M., and Pintar, A. (2015). Nanoshaped CuO/CeO₂ materials: effect of the exposed ceria surfaces on catalytic activity in N₂O decomposition reaction. *ACS Catal.* **5**, 5357–5365.
- Zhan, G., and Zeng, H.C. (2018). Hydrogen spillover through Matryoshka-type (ZIFs@)_n-ZIFs nanocubes. *Nat. Commun.* **9**, 3778.
- Zhang, M., Huang, Z., Zhou, G., Zhu, L., Feng, Y., Lin, T., Hou, H., and Guo, Q. (2015). A sensitive hydrogen peroxide sensor based on a three-dimensional N-doped carbon nanotube-hemin modified electrode. *Anal. Methods* **7**, 8439–8444.
- Zhang, Z., Xiao, J., Chen, X.-J., Yu, S., Yu, L., Si, R., Wang, Y., Wang, S., Meng, X., Wang, Y., et al. (2018). Reaction mechanisms of well-defined metal–N₄ sites in electrocatalytic CO₂ reduction. *Angew. Chem. Int. Ed.* **57**, 16339–16342.

iScience, Volume 23

Supplemental Information

Biomimetic Au/CeO₂ Catalysts Decorated with Hemin or Ferrous Phthalocyanine for Improved CO Oxidation *via* Local Synergistic Effects

Longlong Fan, Jiajun Dai, Zhongliang Huang, Jingran Xiao, Qingbiao Li, Jiale Huang, Shu-Feng Zhou, and Guowu Zhan

iScience

Supporting Information

Biomimetic catalysts with hemin or ferrous phthalocyanine for high-efficient CO oxidation via local synergistic effects

Longlong Fan,^{a,§} Jiajun Dai,^{b,§} Zhongliang Huang,^a Jingran Xiao,^a Qingbiao Li,^{b,c} Jiale Huang,^{b} Shu-Feng Zhou,^{a*} and Guowu Zhan^{a*}*

^a College of Chemical Engineering, Integrated Nanocatalysts Institute (INCI), Huaqiao University, 668 Jimei Avenue, Xiamen, Fujian, 361021, P. R. China

^b Department of Chemical and Biochemical Engineering, College of Chemistry and Chemical Engineering, Xiamen University, 422 South Siming Road, Xiamen, Fujian, 361005, P. R. China

^c College of Food and Biology Engineering, Jimei University, Xiamen, Fujian 361021, P. R. China

Corresponding authors Email:

gwzhan@hqu.edu.cn (G. Zhan)

cola@xmu.edu.cn (J. Huang)

szhou@hqu.edu.cn (S. Zhou)

[§]These authors contributed equally to this work.

Transparent Methods

Materials

The following chemicals were used as received without further purification: gold (III) chloride trihydrate, hemin (ferric protoporphyrin IX chloride, >95%), ferrous phthalocyanine (FePc), polyvinylpyrrolidone (PVP), sodium hydroxide, trimesic acid (H₃BTC), N,N-dimethylformamide (DMF), cerium(III) nitrate hexahydrate, 4-aminobenzenethiol, tetrabutylammonium borohydride (R-NBH₄), methanol, and ethanol. Unless specifically mentioned, all the chemicals were of analytical grade and purchased from Sinopharm Chemical Reagent Co. Ltd.

Synthesis of CeO₂ support

Ce-BTC nanorods were synthesized by a solvothermal method with DMF and ethanol as mixed solvents. Firstly, 50 mL of H₃BTC ethanolic solution (42 g/L), 50 mL of DMF, and 10 mL of PVP ethanolic solution (10 g/L) were mixed before the addition of 50 mL of Ce(NO₃)₃ ethanolic solution (43.4 g/L). The mixture was further stirred for 10 min before heating in an oven at 80 °C for 20 h. After the reaction, white-color products were centrifuged, washed with ethanol three times, and dried at 60°C for 4 h. Subsequently, the CeO₂ was obtained by calcination of Ce-BTC nanorods at a box furnace at 300°C for 3 h with a heating rate of 5 °C/min. The characterization data of Ce-BTC can be found in Figure S4, including N₂ physisorption isotherms, XRD patterns, SEM image, and TGA profile.

Synthesis of hemin-Au/CeO₂ and FePc-Au/CeO₂

For a general synthesis, 0.13 g of the above-prepared CeO₂ was dispersed into 40 mL methanol by sonication for around 10 min. Then, 0.5 mL hemin methanolic solution (4 mg/mL) was added. The mixture was stirred for 10 min at room temperature, followed by the addition of 0.1 mL of HAuCl₄

(48.6 mM) and 0.5 mL of 4-aminothiophenol methanolic solution (28 mM). After stirring for 30 min, 0.15 mL of a freshly prepared R-NBH₄ methanolic solution (0.25 M) was added to the above solution. The mixture was then stirred at room temperature for another 10 min, followed by centrifugation and washing with ethanol twice, and dried at 60°C for 12 h. Similarly, FePc-Au/CeO₂ catalyst was prepared by changing the hemin methanolic solution with the same amount of FePc methanolic solution.

Catalytic performance evaluation method

The catalytic performance of CO oxidation was evaluated in a fixed bed flow microreactor under atmospheric pressure using 0.1 g of catalyst powder after pretreated in N₂ at 170°C for 2 h. The flow rate of the reaction gas (1%CO/4%O₂/95%N₂) was controlled at 20 mL/min by an electronic flowmeter. The temperature was measured with a thermocouple located at the center of the catalyst bed. Both reactant and product compositions were monitored an on-line gas chromatograph (GC-9160) equipped with a thermal conductivity detector.

CO pulse adsorption experiments

CO chemisorption experiments were conducted in a fixed-bed reactor under ambient pressure (Liu et al., 2014). In general, 50 mg of catalyst sample was placed in a quartz reactor and a pure He flow of 50 mL/min was used as the carrier gas, then the samples were pre-treated by He at 170°C for 1h before CO chemisorption. After cooled down to 40°C, the catalyst was flushed with He (30 mL/min) for 1 h at the same temperature. Then pulses of CO were fed into the stream of the carrier gas, and a thermal conductivity detector was used to monitor the amount of CO chemisorption.

Operando DRIFTS experiments

DRIFTS experiments were performed on an IR spectrometer (Thermo, Nicolet iS50), equipped with

a DRIFTS cell (Harrick Scientific) fitted with ZnSe windows and mercury–cadmium–telluride (MCT) detector cooled by liquid N₂. DRIFTS spectra were collected in the range of 2500-1800 cm⁻¹, accumulating 64 scans with a resolution of 4 cm⁻¹. Prior to each test, all samples were heated in N₂ (50 mL/min) from ambient temperature to 170°C at a rate of 10 °C /min and retained at 170 °C for 1 h to remove moisture and impurity adsorbed on the catalyst surface. Then, the samples were cooled down to 30°C and the background spectra were collected after N₂ purging for 30 min in a flow rate of 30 mL/min. Subsequently, the samples were exposed to a flowing CO gas (30 mL/min) and the DRIFTS were recorded until no visible change. After that, N₂ purge at a flow rate of 30 mL/min for 30 min to remove the gaseous and physisorbed CO molecule in the DRIFTS cell, then O₂ (30 mL/min) was introduced into the DRIFTS cell for a certain period. It is worth mentioning that the DRIFTS were recorded until the absorption band intensities reach stable states under every progress.

Materials characterization methods

Size and morphologies of the samples were characterized by field-emission scanning electron microscopy (SEM, JSM-6700F), transmission electron microscopy (TEM, JEM-2010), and high-angle annular dark-field scanning TEM (HAADF-STEM, FEI, Talos F200S). X-ray diffraction (XRD) patterns were recorded on a Rigaku Smart Lab operated at 30 mA and 40 kV using a Cu K α radiation ($\lambda=1.5418$ Å). X-ray photoelectron spectroscopy (XPS) measurement was carried out using a spectrophotometer (AXIS-HSi, Kratos Analytical), wherein the mentioned binding energies were calibrated with C 1s peak (284.8 eV) as a reference. N₂ physisorption isotherms were performed using a static volume analyzer (Quantachrome, Autosorb-iQ) at 77 K. Pulse CO chemisorption was conducted on a gas analyzer (MTP3060 Baidewo instrument) equipped with a

thermal conductivity detector (TCD). Thermal degradation behaviors of the samples were carried out on a thermogravimetric analyzer (TGA, Shimadzu DTG-60H) at a constant heating rate of 10 °C/min. Metal contents in catalyst samples were determined by an inductively coupled plasma optical emission spectrometry (ICP-OES, Agilent 720-ES). Molecular functional groups were characterized by a Fourier transform infrared spectroscopy (FTIR, Thermoscientific Nicolet 6700). Raman spectra were obtained by using a microscopic confocal Raman spectrometer (Renishaw) instrument with an excitation wavelength of 532 nm. UV-vis absorption spectra were recorded on a spectrophotometer (UV-8000A, Shanghai Yuanxi Co. Ltd.)

DFT calculation method

According to the DFT approach within the generalized gradient approximation (GGA),(Kresse and Furthmüller, 1996) the *Vienna ab initio Simulation Package* (VASP) code was used to perform our study. The valence electronic states are expanded in a set of periodic plane waves. Meanwhile, through the projector augmented wave (PAW) method,(Perdew et al., 1996) we implemented the interaction among core electrons and valence electrons. In addition, the convergence thresholds have been set to 10^{-5} eV and 10^{-3} eV/Å for the input energy and the force, respectively. The interactions of the periodic images were avoided by employing a vacuum space larger than 25 Å along the Z direction. The Brillouin zone On-site coulomb interactions of Ce 4f electrons were employed to demonstrate the DFT + U with the value of $U_{\text{eff}}(\text{Ce}) = 4.5$ eV.(Dai et al., 2020) The adsorption energy of reactant gas was calculated through the following formula: $E_{\text{ad}} = E(\text{gas/catalyst}) - E(\text{gas}) - E(\text{catalyst})$, based on the single-point free energy of the relaxed geometries with the same computational settings. The formation energy of an oxygen vacancy, E_{vac} , was estimated by the formula $E_{\text{vac}} = E(\text{CeO}_{2-x}) + 1/2 \times E(\text{O}_2) - E(\text{CeO}_2)$, where $E(\text{CeO}_{2-x})$ represents the energy of the

partially reduced ceria (111) with an oxygen vacancy. $E(\text{CeO}_2)$ and $E(\text{O}_2)$ are the energies of optimal stoichiometric ceria surface and a gas phase O_2 molecule, respectively.

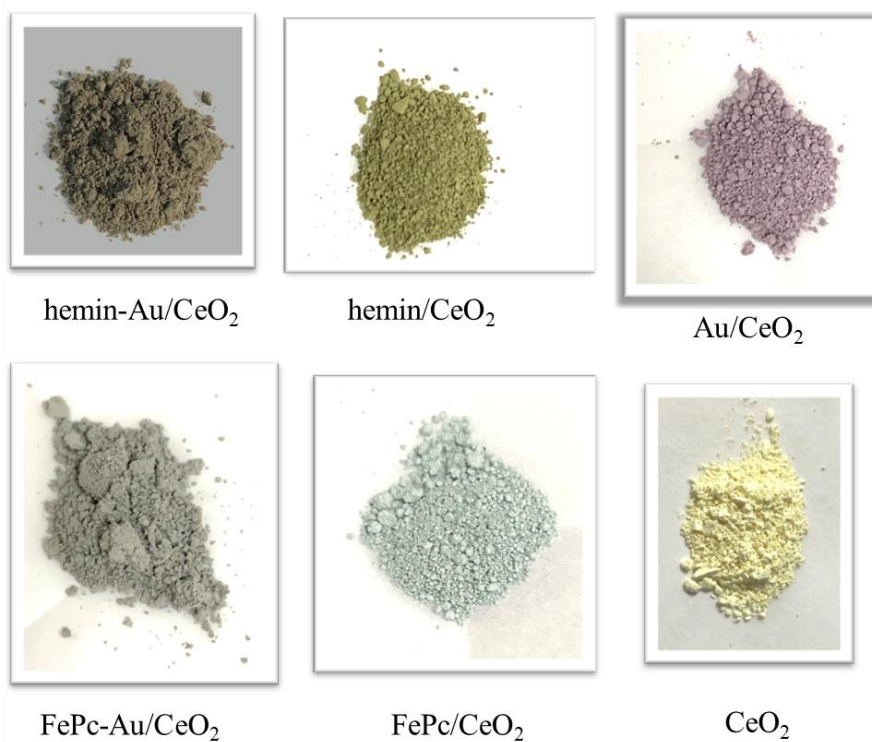


Figure S1. Digital photos of CeO₂ support and the various supported catalysts. Related to Figure 1.

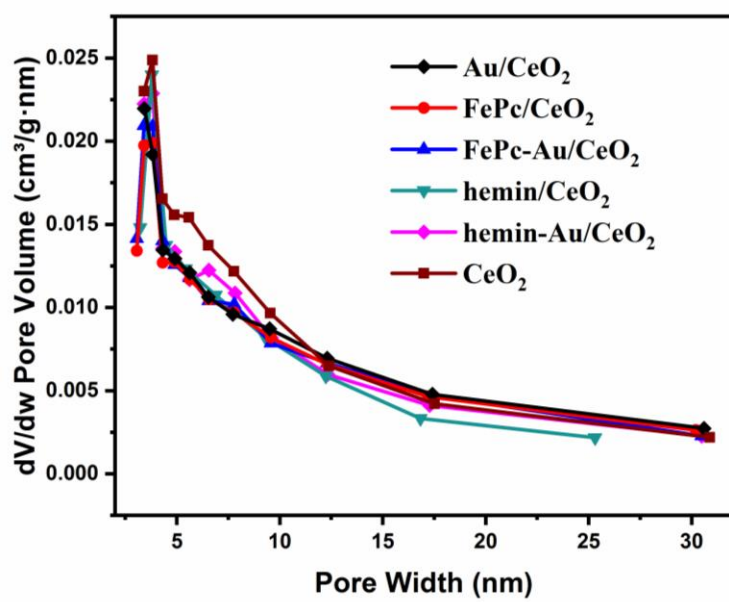


Figure S2. Pore size distributions of the different samples. Related to Figure 1.

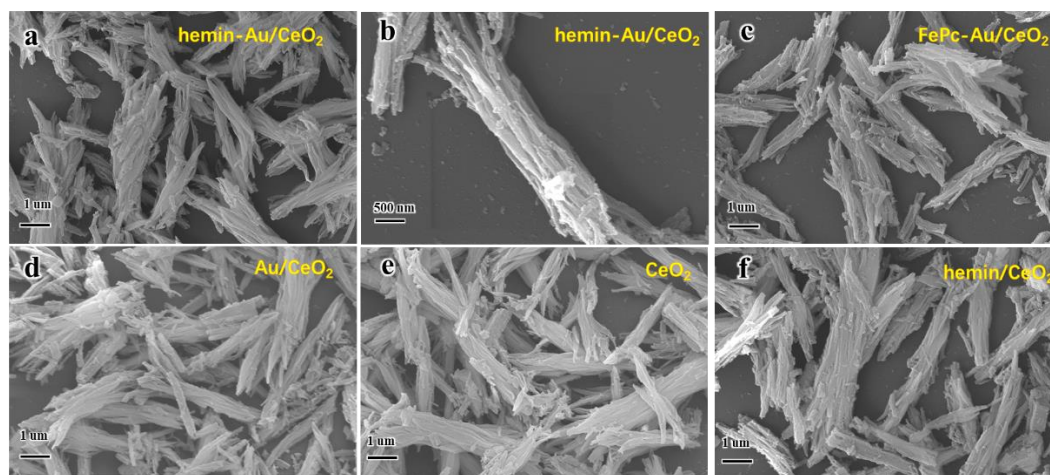


Figure S3. Representative SEM images of the catalyst samples. (a, b) hemin-Au/CeO₂, (c) FePc-Au/CeO₂, (d) Au/CeO₂, (e) CeO₂, and (f) hemin/CeO₂. Related to Figure 2.

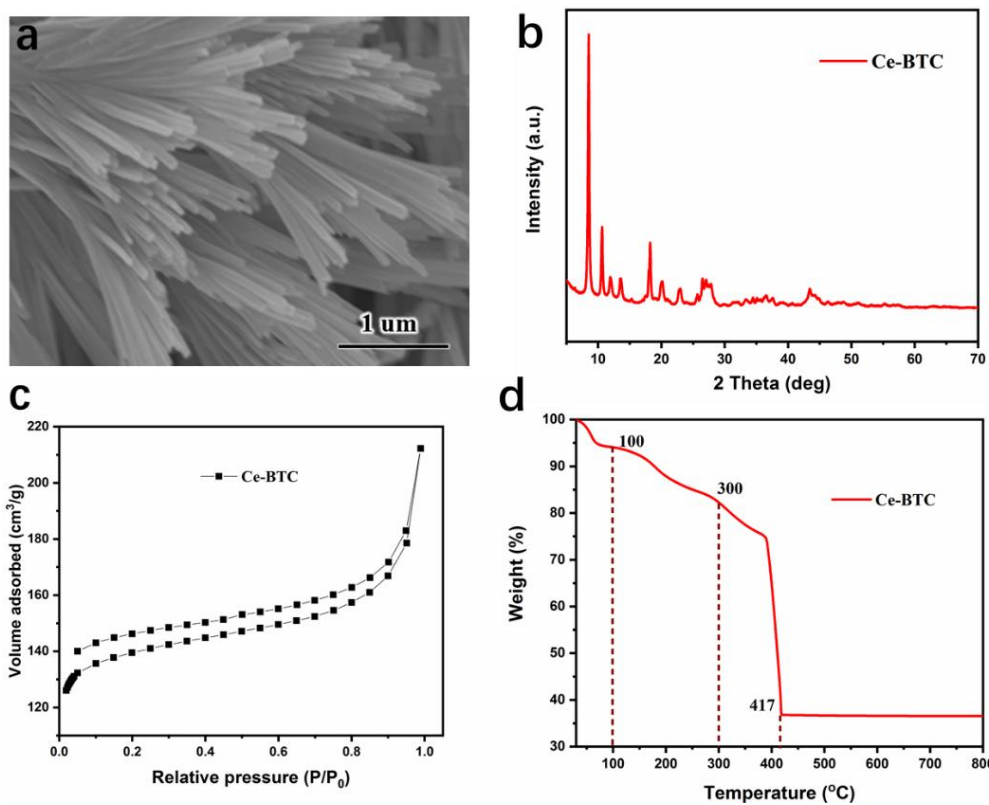


Figure S4. Characterization results of the original Ce-BTC. (a) SEM image, (b) XRD pattern, (c) N₂ physisorption isotherms, and (d) TGA profile. Related to Figure 2.

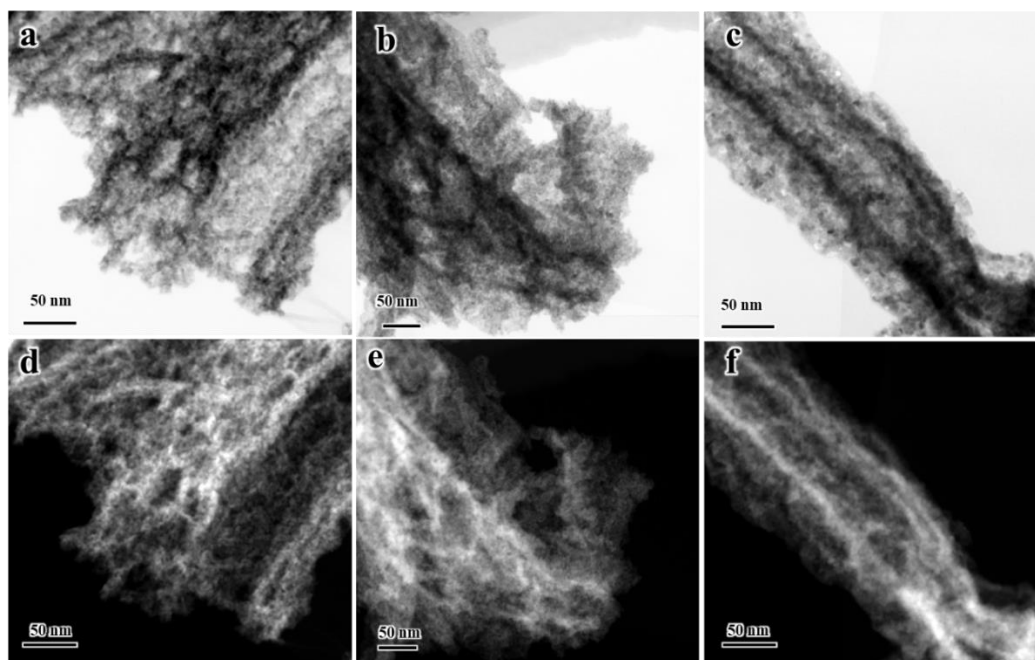


Figure S5. More characterization data of the hemin-Au/CeO₂ catalyst. (a-c) TEM images and (d-f) HAADF-STEM images. Related to Figure 2.

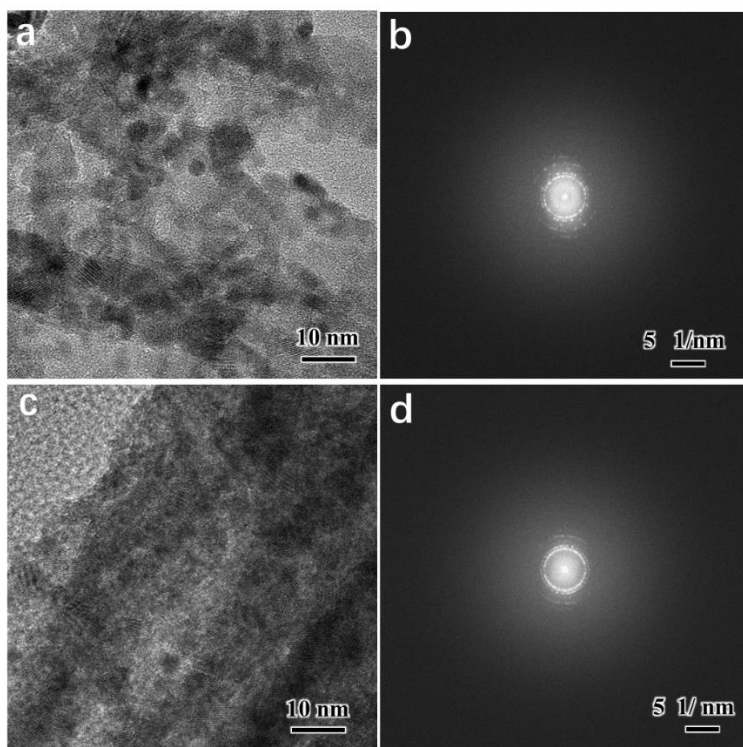


Figure S6. TEM images and the corresponding SAED patterns of the catalyst samples. (a, b) Au/CeO₂, and (c, d) FePc-Au/CeO₂. Related to Figure 2.

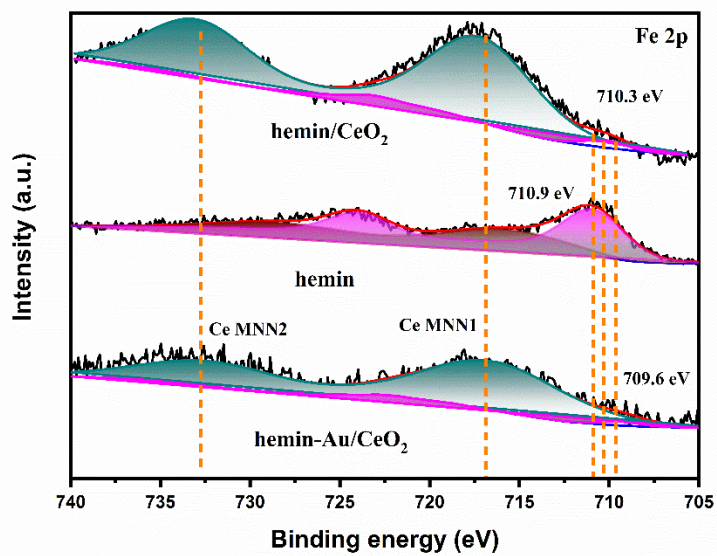


Figure S7. High-resolution XPS spectra in the Fe2*p* region of different samples. Related to Figure 3.

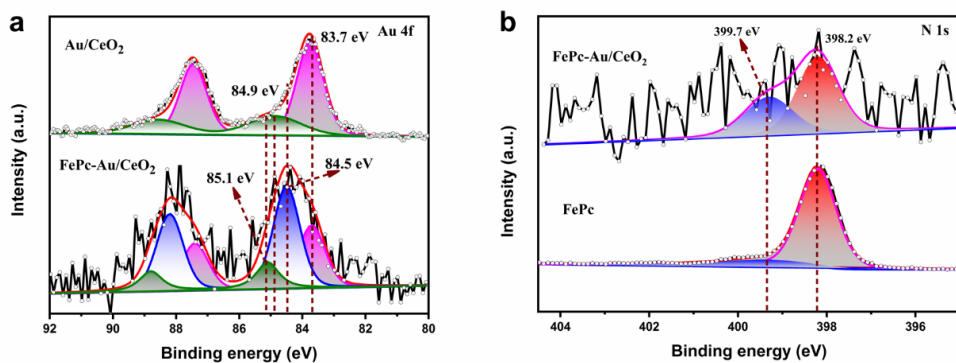


Figure S8. High-resolution XPS spectra of FePc-Au/CeO₂ catalyst. (a) Au 4f and (b) N 1s. Related to Figure 3.

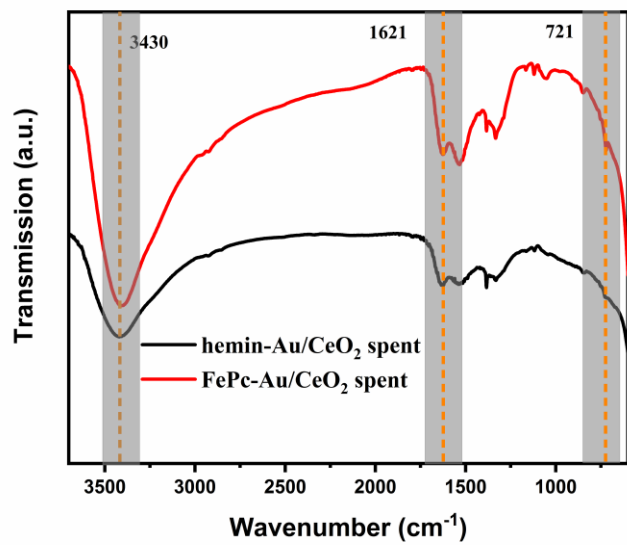


Figure S9. FTIR spectra of the spent catalysts after CO oxidation reaction. Related to Figure 4.

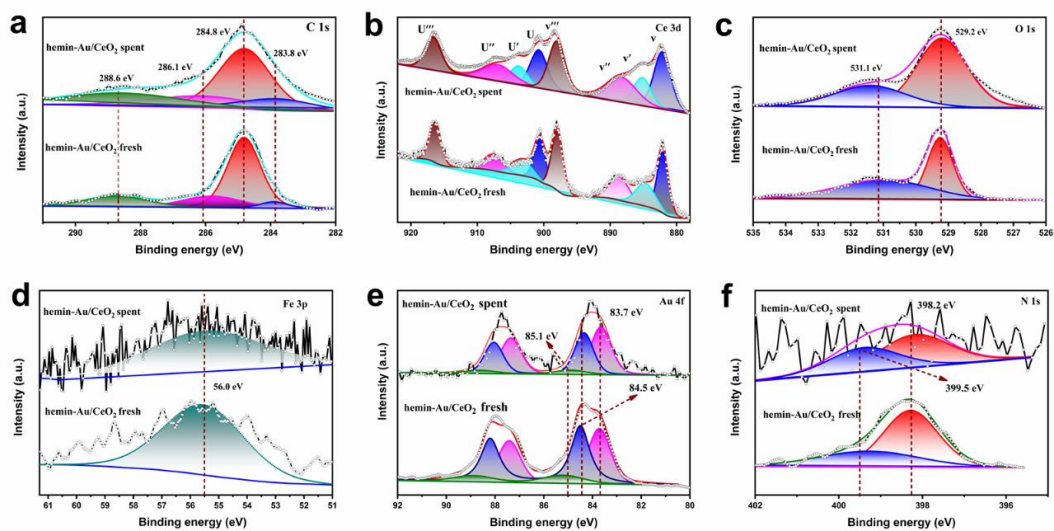


Figure S10. XPS spectra of the fresh and spent hemin-Au/CeO₂ catalysts after the long-term test (240 h). (a) C 1s, (b) Ce 3d, (c) O 1s, (d) Fe 3p, (e) Au 4f, and (f) N 1s. Related to Figure 3.

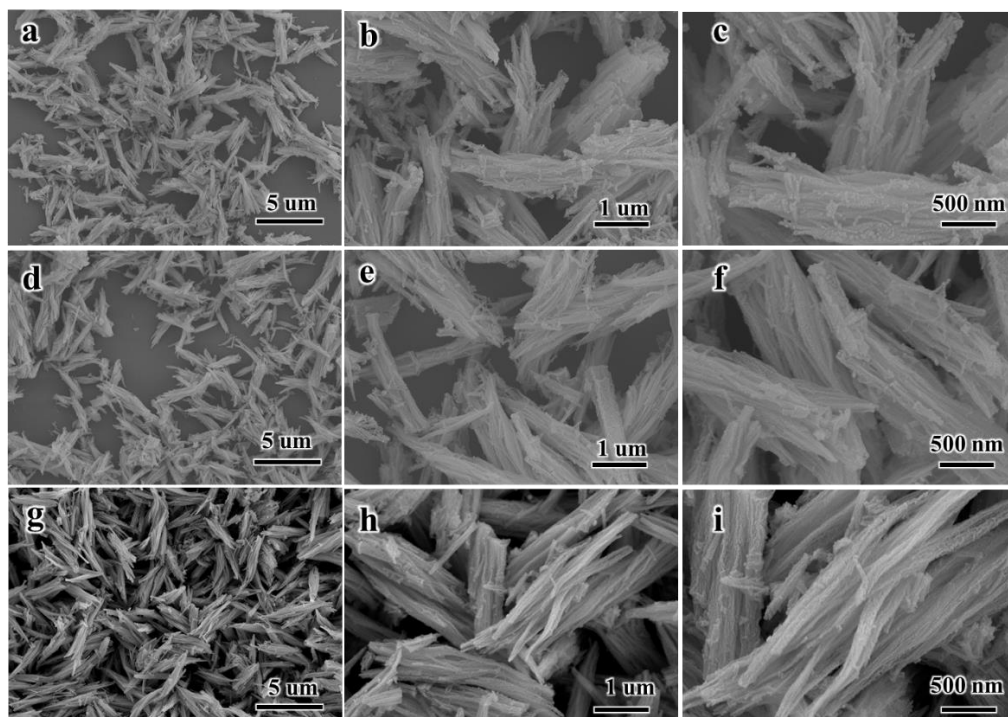


Figure S11. SEM images of the spent catalysts after the CO oxidation reaction. (a-c) Au/CeO₂ catalyst, (d-f) hemin-Au/CeO₂ catalyst, and (g-i) FePc-Au/CeO₂ catalyst. Related to Figure 4.

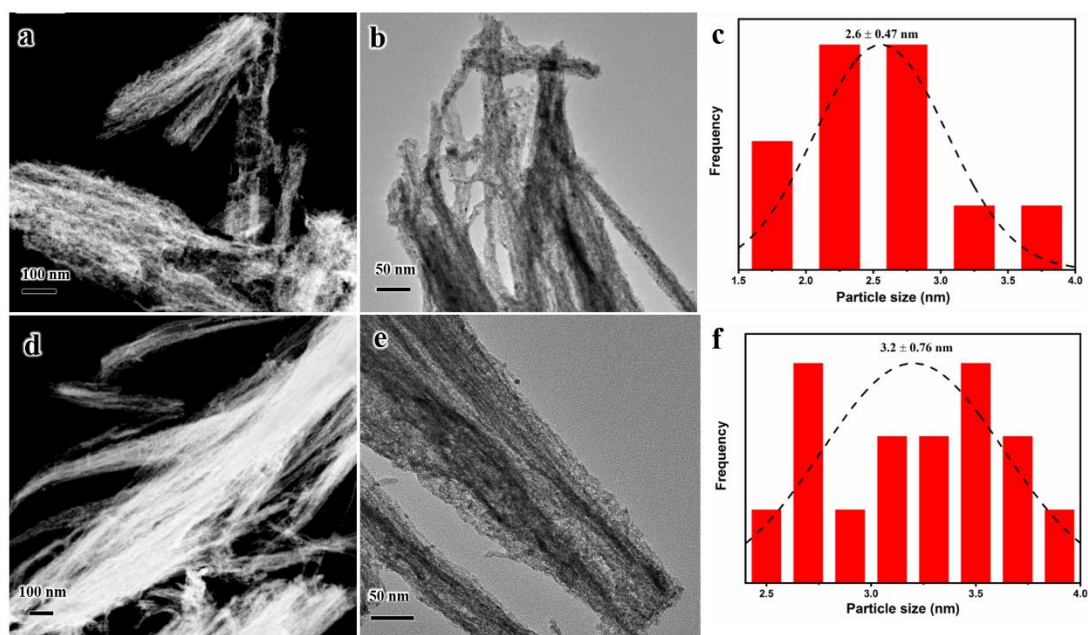


Figure S12. Characterization results of the spent catalysts (after the long-term evaluation at 80°C for 240 h) including HAADF-STEM images, TEM images, and particle size distribution histograms of the supported Au nanoparticles. (a-c) hemin-Au/CeO₂, and (d-f) FePc-Au/CeO₂. Related to Figure 4.

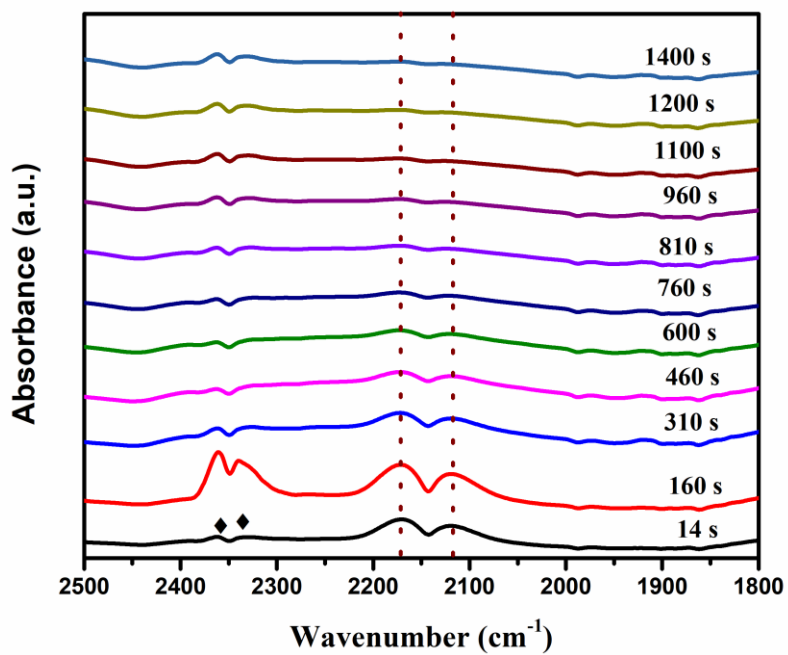


Figure S13. Time-dependent IR spectra during the oxidation of adsorbed CO over the Au/CeO₂ catalyst at 30°C. Related to Figure 5.

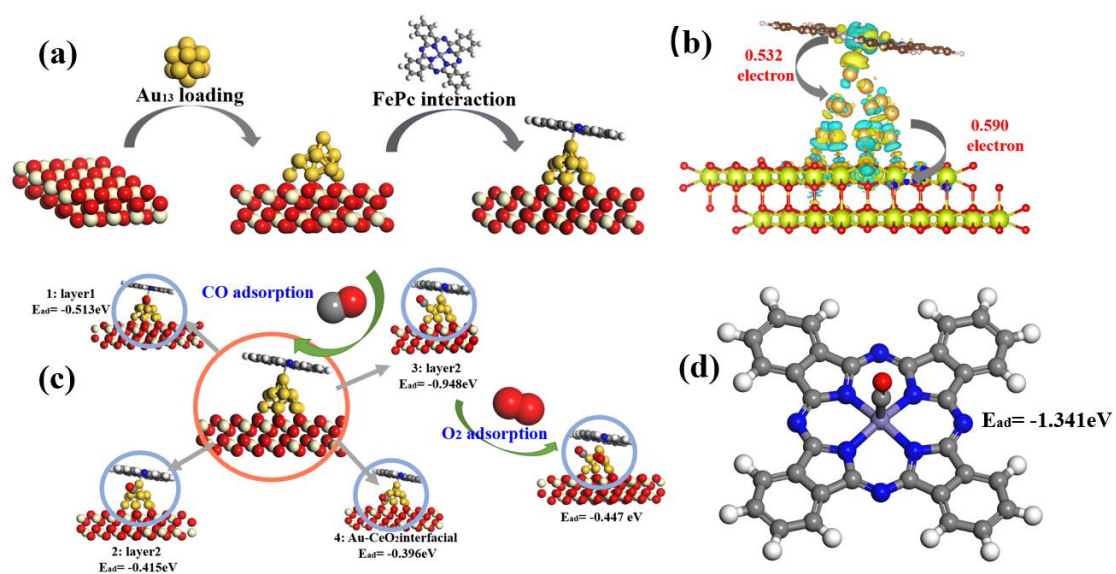


Figure S14. DFT calculation results of the FePc-Au/CeO₂ system. (a) The catalyst model, (b) Bader charge analysis, (c) schematic illustrations of the various CO adsorption sites and co-adsorbed O₂ on FePc-Au/CeO₂, and (d) schematic illustration of CO adsorption on FePc. Related to Figure 6.

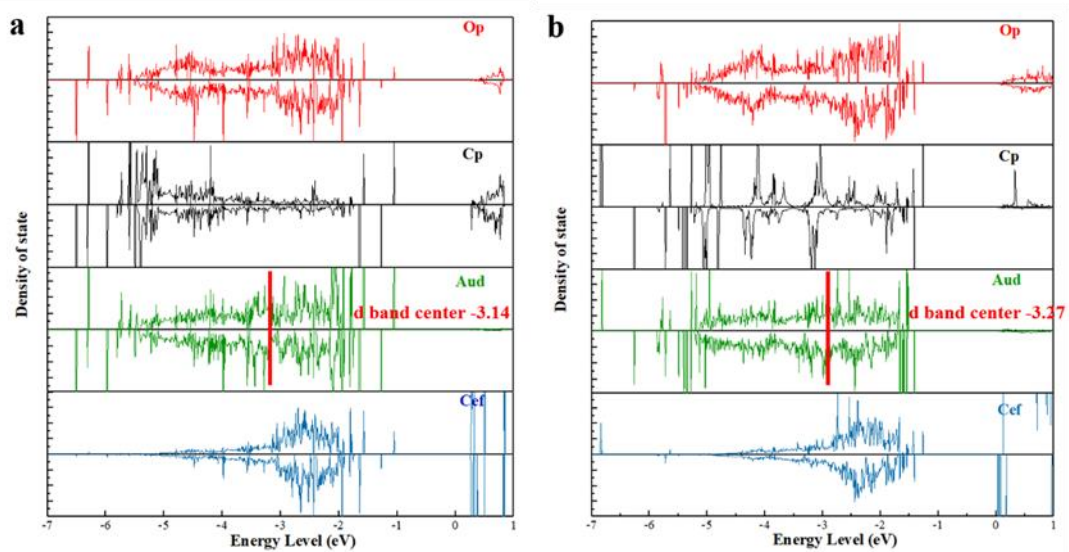


Figure S15. Partial density of states of the catalyst samples. (a) Au-CeO₂, (b) hemin-Au/CeO₂. Related to Figure 7.

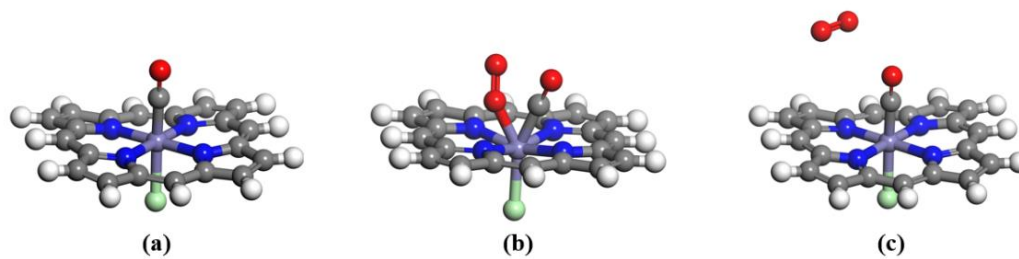


Figure S16. The structural models used in DFT calculations. (a) CO adsorption on hemin, (b) CO and O₂ co-adsorption on hemin, and (c) the result of co-adsorption simulation showing the expelling of oxygen molecule. Related to Figure 7.

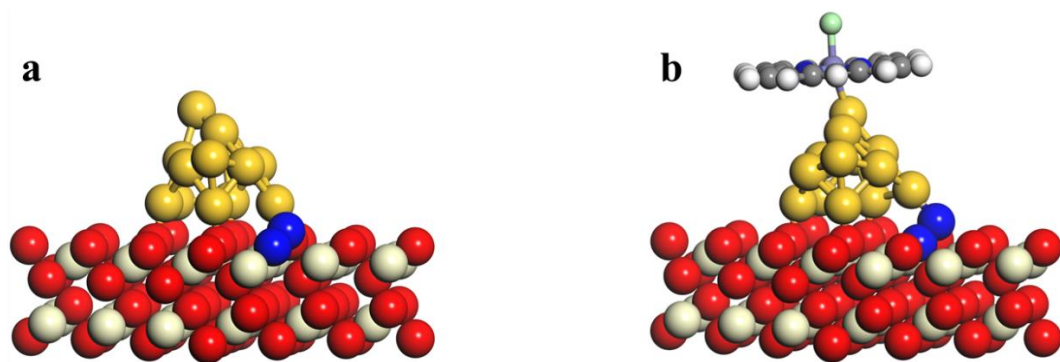


Figure S17. The structural models used in DFT calculations. (a) O₂ adsorbed on the oxygen vacancy of Au/CeO₂ and (b) O₂ adsorbed on the oxygen vacancy of hemin-Au/CeO₂. Related to Figure 8.

Table S1. Catalytic performance comparison of various Au based catalysts for CO oxidation reaction. Related to Figure 4.

Catalyst	Gas hourly space velocity (mL h ⁻¹ g _{cat} ⁻¹)	T ₁₀₀ (°C)	Reference
Au/CeO ₂	20000	78	(Wang et al., 2016)
Au@ZIF-8	9600	90	(Jiang et al., 2009)
Au/HKUST-1	25000	190	(Liu et al., 2016)
Au-Pt/TiO ₂	10890	80	(Li et al., 2018)
Ir-Au/Al ₂ O ₃	100000	250	(Song et al., 2013)
Au/Fe ₂ O ₃	12000	250	(Tanaka et al., 2018)
Au@TiO ₂	21780	>260	(Chen et al., 2010)
Au/Ce/HMS	20000	250	(Hernandez et al., 2009)
Au/LaMnO ₃	9000	90	(Jia et al., 2011)
Au/ZnO	15000	250	(Carabineiro et al., 2010)
Au-Cu/Ce-BTC	12000	50	(Fan et al., 2019)
AuCu _{0.1} Ce _{0.85} Zr _{0.05} O ₂	6000	36	(Gnanakumar et al., 2014)
Au/CuO/(oyster shell)	38000	150	(Liu et al., 2019)
Au/CeO ₂	6000	125	(Bezkrvnyi et al., 2019)
Au-CuO _x /boron nitride	80400	80	(Wu et al., 2021)
hemin-Au/CeO ₂	12000	70	this work
FePc-Au/CeO ₂	12000	70	this work

References

- Bezkravnyy, O., Kraszkiewicz, P., Krivtsov, I., Quesada, J., Ordóñez, S., Kepinski, L., (2019). Thermally induced sintering and redispersion of Au nanoparticles supported on Ce_{1-x}EuxO₂ nanocubes and their influence on catalytic CO oxidation. *Catal. Commun.* *131*, 105798.
- Carabineiro, S.A.C., Machado, B.F., Bacsá, R.R., Serp, P., Dražić, G., Faria, J.L., Figueiredo, J.L., (2010). Catalytic performance of Au/ZnO nanocatalysts for CO oxidation. *J. Catal.* *273*, 191-198.
- Chen, Y., Zhu, B., Yao, M., Wang, S., Zhang, S., (2010). The preparation and characterization of Au@TiO₂ nanoparticles and their catalytic activity for CO oxidation. *Catal. Commun.* *11*, 1003-1007.
- Dai, J., Guo, Y., Xu, L., Zhuang, G., Zheng, Y., Sun, D., Huang, J., Li, Q., (2020). Bovine serum albumin templated porous CeO₂ to support Au catalyst for benzene oxidation. *Mol. Catal.* *486*, 110849.
- Fan, L.L., Zhao, F.G., Huang, Z.L., Chen, B., Zhou, S.F., Zhan, G.W., (2019). Partial deligandation of M/Ce-BTC nanorods (M = Au, Cu, Au-Cu) with "Quasi-MOF" structures towards improving catalytic activity and stability. *Appl. Catal. A* *572*, 34-43.
- Gnanakumar, E.S., Naik, J.M., Manikandan, M., Raja, T., Gopinath, C.S., (2014). Role of Nanointerfaces in Cu- and Cu plus Au-Based Near-Ambient-Temperature CO Oxidation Catalysts. *ChemCatChem* *6*, 3116-3124.
- Hernandez, J.A., Gómez, S., Pawelec, B., Zepeda, T.A., (2009). CO oxidation on Au nanoparticles supported on wormhole HMS material: Effect of support modification with CeO₂. *Appl. Catal. B* *89*, 128-136.
- Jia, M., Li, X., Zhaorigetu, Shen, Y., Li, Y., (2011). Activity and deactivation behavior of Au/LaMnO₃ catalysts for CO oxidation. *J. Rare Earth.* *29*, 213-216.
- Jiang, H.L., Liu, B., Akita, T., Haruta, M., Sakurai, H., Xu, Q., (2009). Au@ZIF-8: CO oxidation over gold nanoparticles deposited to metal-organic framework. *J. Am. Chem. Soc.* *131*, 11302-11303.
- Kresse, G., Furthmüller, J., (1996). Efficient iterative schemes for ab initio total-energy calculations using a plane-wave basis set. *Phys. Rev. B* *54*, 11169-11186.
- Li, J.-J., Zhu, B.-L., Wang, G.-C., Liu, Z.-F., Huang, W.-P., Zhang, S.-M., (2018). Enhanced CO catalytic oxidation over an Au-Pt alloy supported on TiO₂ nanotubes: investigation of the hydroxyl and Au/Pt ratio influences. *Catalysis Science & Technology* *8*, 6109-6122.
- Liu, H.-H., Wang, Y., Jia, A.-P., Wang, S.-Y., Luo, M.-F., Lu, J.-Q., (2014). Oxygen vacancy promoted CO oxidation over Pt/CeO₂ catalysts: A reaction at Pt-CeO₂ interface. *Appl. Surf. Sci.* *314*, 725-734.
- Liu, X., Dai, J.J., Li, W., Wang, K.C., Huang, J.L., Li, Q.B., Zhan, G.W., (2019). Green Fabrication of Integrated Au/CuO/Oyster Shell Nanocatalysts with Oyster Shells as Alternative Supports for CO Oxidation. *ACS Sustainable Chem. Eng.* *7*, 17768-17777.
- Liu, Y., Zhang, J., Song, L., Xu, W., Guo, Z., Yang, X., Wu, X., Chen, X., (2016). Au-HKUST-1 Composite Nanocapsules: Synthesis with a Coordination Replication Strategy and Catalysis on CO Oxidation. *ACS Appl. Mater. Interfaces* *8*, 22745-22750.
- Perdew, J.P., Burke, K., Ernzerhof, M., (1996). Generalized gradient approximation made simple. *Phys. Rev. Lett.* *77*, 3865-3868.
- Song, Y.-J., López-De Jesús, Y.M., Fanson, P.T., Williams, C.T., (2013). Preparation and Characterization of Dendrimer-Derived Bimetallic Ir-Au/Al₂O₃ Catalysts for CO Oxidation. *J. Phys. Chem. C* *117*, 10999-11007.
- Tanaka, S., Lin, J., Kaneti, Y.V., Yusa, S.I., Jikihara, Y., Nakayama, T., Zakaria, M.B., Alshehri, A.A., You, J., Hossain, M.S.A., Yamauchi, Y., (2018). Gold nanoparticles supported on mesoporous iron oxide

for enhanced CO oxidation reaction. *Nanoscale* 10, 4779-4785.

Wang, Z., Fu, H., Tian, Z., Han, D., Gu, F., (2016). Strong metal-support interaction in novel core-shell Au-CeO₂ nanostructures induced by different pretreatment atmospheres and its influence on CO oxidation. *Nanoscale* 8, 5865-5872.

Wu, F., He, L., Li, W.-C., Lu, R., Wang, Y., Lu, A.-H., (2021). Highly dispersed boron-nitride/CuOx-supported Au nanoparticles for catalytic CO oxidation at low temperatures. *Chinese Journal of Catalysis* 42, 388-395.